Seasonal tracer subduction in the Subpolar North Atlantic driven by submesoscale fronts

Théo Picard[1], Jonathan Gula[1], Clement Vic[2], and Laurent Mémery[3]

[1]Université de Bretagne Occidentale
[2]Laboratoire d'Oceanographie Physique et Spatiale, University of Brest, CNRS, IRD, Ifremer
[3]LEMAR

December 7, 2023

Abstract

Submesoscale flows (0.1 - 10 km) are often associated with large vertical velocities, which can have a significant impact on the transport of surface tracers, such as carbon. However, global models do not adequately account for these small-scale effects, which still require a proper parameterization. In this study, we introduced a passive tracer into the mixed layer of the northern Atlantic Ocean using a CROCO simulation with a high horizontal resolution of $\Delta x = 800$ m, aiming to investigate the seasonal submesoscale effects on vertical transport. Using surface vorticity and strain criteria, we identified regions with submesoscale fronts and quantified the associated subduction, that is the export of tracer below the mixed layer depth. The results suggest that the tracer vertical distribution and the contribution of frontal subduction can be estimated from surface strain and vorticity. Notably, we observed significant seasonal variations. In winter, the submesoscale fronts contribute up to 40% of the vertical advective transport of tracer below the mixed layer, while representing only 5% of the domain. Conversely, in summer, fronts account for less than 1% of the domain and do not contribute significantly to the transport below the mixed layer. The findings of this study contribute to a better understanding of the seasonal water subduction due to fronts in the region.

Seasonal tracer subduction in the Subpolar North Atlantic driven by submesoscale fronts

Théo Picard[1], Jonathan Gula[2,3], Clément Vic[2], Laurent Mémery [1]

[1]Univ Brest, CNRS, IRD, Ifremer, Laboratoire des Sciences de l'Environnement Marin (LEMAR), IUEM, Plouzané, France
[2]Univ Brest, CNRS, IRD, Ifremer, Laboratoire d'Océanographie Physique et Spatiale (LOPS), IUEM, Plouzané, France
[3]Institut Universitaire de France (IUF), Paris, France

Key Points:

- Surface strain and vorticity criteria can be used to identify submesoscale fronts.
- The tracer depth injection correlates with density of fronts, regardless of the mixed layer depth evolution.
- The submesoscale fronts contribute to $\sim 40\%$ of the vertical advective subduction in winter, and less than 1% in summer.

Corresponding author: Théo Picard, `theo.picard@univ-brest.fr`

Abstract

Submesoscale flows (0.1 - 10 km) are often associated with large vertical velocities, which can have a significant impact on the transport of surface tracers, such as carbon. However, global models do not adequately account for these small-scale effects, which still require a proper parameterization. In this study, we introduced a passive tracer into the mixed layer of the northern Atlantic Ocean using a CROCO simulation with a high horizontal resolution of $\Delta x = 800$ m, aiming to investigate the seasonal submesoscale effects on vertical transport. Using surface vorticity and strain criteria, we identified regions with submesoscale fronts and quantified the associated subduction, that is the export of tracer below the mixed layer depth. The results suggest that the tracer vertical distribution and the contribution of frontal subduction can be estimated from surface strain and vorticity. Notably, we observed significant seasonal variations. In winter, the submesoscale fronts contribute up to 40% of the vertical advective transport of tracer below the mixed layer, while representing only 5% of the domain. Conversely, in summer, fronts account for less than 1% of the domain and do not contribute significantly to the transport below the mixed layer. The findings of this study contribute to a better understanding of the seasonal water subduction due to fronts in the region.

Plain Language Summary

Small ocean movements known as submesoscale fronts are often overlooked in global models. These flows, ranging from 0.1 to 10 kilometers, play a big role in how carbon, nutrient or heat are transported inside the ocean. To better understand the influence of submesoscale fronts, we use a fine scale numerical simulations in the North Atlantic. We added a tracer in the ocean upper-layer to analyse how it gets transported at depth. Using criteria of surface rotation speed and how water gets stretched, we identify the areas of submesoscale fronts. We observed that the depth at which the tracer is injected depend on the density of submesoscale fronts. Also, the study results show that these flows exhibit interesting seasonal variations. In winter, the submesoscale fronts contribute up to 40% to the vertical transport of carbon, even though they only cover 5% of the studied area. Conversely, in summer, fronts represent less than 1% of the area and don't significantly impact the vertical tracer transport. This study helps us better understand how water moves in the ocean, especially across different seasons. This understanding could be key to addressing questions related to climate change and how substances like carbon are distributed in the world's oceans.

1 Introduction

There is an on-growing set of evidence that submesoscale physical processes actually matter for the transport of oceanic tracers such as heat, carbon and nutrients (Klein & Lapeyre, 2009; Omand et al., 2015; Stukel et al., 2017; Llort et al., 2018; Lévy et al., 2018; Boyd et al., 2019; Lacour et al., 2019). Submesoscale phenomena are characterised by frontal and filamentary structures with lateral scales ranging from 1 to 10 km. These structures typically arise from mesoscale eddy stirring and baroclinic instability at the ocean surface, exhibiting Rossby ($Ro = \zeta/f$) numbers on the order of 1 (Lévy et al., 2024). The frontogenesis, responsible for ageostrophic flow known as secondary circulation, induces strong and deep vertical velocities localised precisely at the front (McWilliams, 2021; Gula, Taylor, et al., 2021). Fronts are characterised by a dense cyclonic side with downward velocities and a light anticyclonic side with upward velocities. In the context of the carbon cycle, this results in a double contribution : On the one hand, it drives nutrients, essential for the primary production, from the (interior) twilight zone into the euphotic layer (Lapeyre Guillaume, 2006; Lévy et al., 2018; Mahadevan, 2016). On the other hand, it facilitates the subduction of surface carbon (transport below the mixed layer) along isopycnal pathways, effectively storing it for extended periods (Wenegrat et al., 2020; Mahadevan et al., 2020; Freilich & Mahadevan, 2021). Concerning heat transport, L. Siegelman et al. (2020) demonstrated that fronts actively participate in the upward heat transport from the ocean interior to the surface and are essential ingredients of the Earth's heat budget.

While it is clear that fronts play a significant role in tracer budgets, the vertical transport induced by submesoscale processes remains unresolved and is not yet parameterized in climate models (Bopp et al., 2013; Mahadevan et al., 2020). Overcoming this challenge is one of the major hurdles in ocean modeling (Fox-Kemper et al., 2019). However, although there has been recent interest in quantifying the submesoscale contribution to tracer transport, there is still no clear consensus on its impact. A major obstacle is the difficulty of sampling submesoscale processes using remote sensing and in situ observational instruments. Indeed, satellite altimetry can only detect structures larger than 100 kilometers (Chelton et al., 2011), and the measurement of vertical transport due to small-scale phenomena in the ocean remains a challenge (Mahadevan et al., 2020). The computation of submesoscale velocity gradient generally requires multiple ships, autonomous underwater vehicles, or surface drifters (Shcherbina et al., 2013; Gula, Taylor, et al., 2021). With respect to numerical simulations, it has been shown that fine-scale ocean regional circulation models with subkilometer horizontal grid spacing can accurately capture submesoscale dynamics (Mahadevan & Tandon, 2006; Capet et al., 2008; Pietri et al., 2021). However, high-resolution modeling is constrained by computational costs (Lévy et al., 2024), resulting in spatial limitations and/or idealized setups.

Various methodologies have been proposed to assess the frontal contribution, particularly in the context of carbon export. Balwada et al. (2018) estimated that the subduction could be doubled by comparing models with 20 and 1 km horizontal resolution. Uchida et al. (2019) quantified the ageostrophic contribution using spectral analysis and found that submesoscale structures could account for about a third of the total fluxes. In Freilich and Mahadevan (2021), Lagrangian particles were used to identify particles trapped in submesoscale structures. Their findings showed that 7.7% of the particles are subducted from the mixed layer, with subduction occurring mainly in localized regions along fronts. Based on glider observations during the North Atlantic bloom and supported by numerical modeling, Omand et al. (2015) showed that submesoscale structures can contribute up to half of the total spring export of particulate organic carbon (POC). In a recent study, Balwada et al. (2021) used Joint Probability Density Function (JPDF) of surface vorticity and strain on an idealized fine-scale model of the Antarctic Circumpolar Current to identify fronts. Their research showed that submesoscale fronts, although occupying only about 5% of the surface domain, could potentially account for up to 20% of the vertical transport at the Mixed Layer Depth (MLD). This wide range of results underlines the complexity and considerable uncertainties associated with this topic.

Despite this growing body of literature, there is a notable gap in knowledge as most studies tend to overlook the seasonal variability of these phenomena. However, it is now clear that submesoscales exhibit a strong seasonal cycle (Callies et al., 2015; Rocha et al., 2016; Berta et al., 2020). Futhermore, the modulation of tracer export on seasonal time scales has recently been demonstrated (Cao & Jing, 2022; Mahadevan et al., 2020). Therefore, the primary objective of our study is to assess the seasonal impact of submesoscale processes on a passive tracer released in the mixed layer (ML) using a highly realistic model. In particular, we focus on the North Atlantic subpolar gyre, a region known for significant seasonal variations. Moreover, this region is particularly important as being one of the most critical areas for carbon sequestration, with an average uptake of about $0.55{-}1.94 PgCyear^{-1}$, which represents $\sim 12\%$ of the global net ocean uptake (Takahashi et al., 2002; Sanders et al., 2014), and with significant phytoplankton blooms in spring, when submesoscale activity is intense (Treguier et al., 2005; Le Corre et al., 2020).

The outline of this paper is as follows. Section 2 presents our numerical simulation. Section 3 outlines the methodology used to identify seasonal surface submesoscale fronts.

Section 4 describes the seasonal evolution of a tracer released within the ML and analyzes the contribution of fronts to tracer subduction. Finally, section 5 provides a detailed discussion of the results.

2 Methodology

2.1 Numerical setup

We set up a realistic simulation of the circulation in a northeastern part of the North Atlantic subpolar gyre, using the oceanic modeling system CROCO (Coastal and Regional Ocean COmmunity model), which resolves the primitive equations (Shchepetkin & McWilliams, 2005). A nesting approach is used here with a parent simulation (GIGATL3) covering most of the Atlantic Ocean with a horizontal resolution of 3 km (Gula, Theetten, et al., 2021). GIGALT3 provides the nested simulation with the initial state and the lateral boundary conditions. The study domain is shown in Figure 1. It covers an area of 800 km × 640 km, ranging from 53.8 N to 62.5°N and from 20.5°W to 37.8°W. The horizontal grid spacing $\Delta x = 800$ m is almost constant across the domain. Vertically, we discretize the model with 200 sigma levels, which roughly corresponds to cell heights of $\Delta z = 2$ m within the surface layer. This vertical resolution is chosen to accurately represent the surface dynamics. The ocean is forced at the surface by hourly atmospheric forcings from the Climate Forecast System Reanalysis using a bulk formulation with relative winds (Saha et al., 2010). Tidal forcing is not included. The grid bathymetry is from the global SRTM30plus dataset (J. J. Becker D. T. Sandwell & Weatherall, 2009). The simulation is run for 13 months, from December 1, 2007, to December 31, 2008, with a time step of 90 seconds and produces 3-hourly averaged outputs. The first month is dedicated to the spin-up phase, ensuring that submesoscale structures have time to develop. We therefore analyse the outputs for the year 2008. To discard boundary effects, all the results are computed within a subdomain excluding points within 100 km of the boundaries.

2.2 Tracer initialisation and equation

On the first day of each month, a passive tracer is released throughout the entire domain within the upper mixed layer (ML) and remains for a period of 29 days. This experimental design allows us to evaluate and compare both ML water subduction and deep export independently for each month. The MLD is determined by computing a density threshold of 0.03 kg m^{-3} from the surface, as described in de Boyer Montégut et al. (2004). We distribute the tracer concentration C following a hyperbolic tangent profile:

$$C(x, y, z, t = 0) = \frac{1}{2}\left(1 + \tanh\left(\frac{z - z_{target}}{dz(x, y)}\right)\right). \qquad (1)$$

Where x, y, z are the spatial coordinates, and t is the time. We choose $z_{target} = 0.6 \cdot z_{mld}(x, y)$ to ensure that there is no tracer below the MLD. In addition, $dz = \frac{-z_{mld}(x,y)}{8}$ is chosen to achieve a smooth transition near the MLD to avoid numerical instability due to sharp vertical gradients in tracer concentration. Figure 2 shows an example of the tracer concentration for 3 selected days in February. It illustrates how the tracer is stirred by the mesoscale and submesoscale circulation and how it accumulates or is depleted from frontal regions.

The CROCO model uses the following tracer equation:

$$\frac{\partial C}{\partial t} = -u_j \frac{\partial C}{\partial x_j} - w \frac{\partial C}{\partial z} + \nu_c + D_c + S_c, \qquad (2)$$

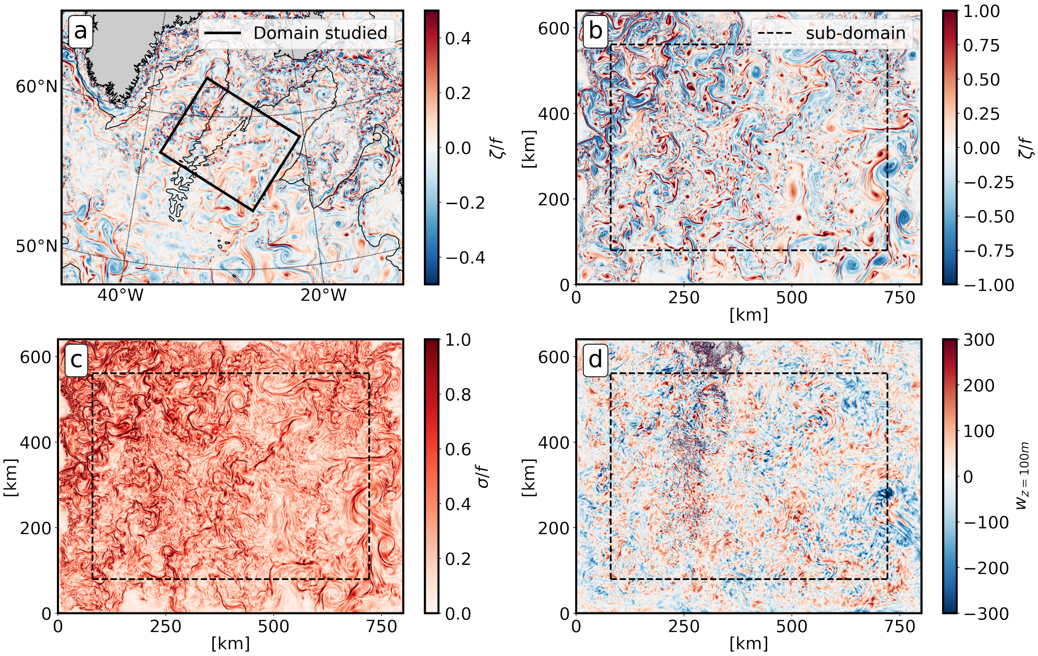

Figure 1. (a) Snapshot of the GIGATL3 simulation (dx = 3km) on the 8th of February . The background is the relative vorticity and the black contour is the bathymetry at 2000 m. The black rectangle is the domain of the regional simulation. (b), (c) and (d) represent the relative vorticity, the strain and vertical velocities at 100 m depth, respectively, computed from the regional simulation (dx = 800m). The relative vorticity and strain are normalised to the local Coriolis frequency. All the statistical results are computed in the dashed rectangle subdomain to discard boundary effects.

where C is the tracer concentration, u_j are the horizontal velocities, w is the vertical velocity, ν_c is the vertical diffusion, D_c is the horizontal diffusion and S_c is a source or sink term (set to zero in this study). D_c is not explicit in CROCO, but results from the implicit contribution of the upstream-biased advection scheme. Vertical mixing ($\nu_c = \frac{\partial}{\partial z}(K_c \frac{\partial C}{\partial z})$ computed with the tracer diffusivity K_c is parameterized with the KPP scheme (Large et al., 1994).

3 Seasonality of submesoscale fronts

The numerical simulation provides compelling evidence for tracer subduction driven by fronts. Figure 3 presents a vertical section of the domain on April 3rd, 3 days after the tracer release. The vertical section highlights a distinct front characterized by a significant increase in vertical velocity (w > 100 m/d) and a pronounced subduction of the tracer below the mixed layer. In this section, we first explain how we identify submesoscale fronts based on a strain and vorticity criterion and we present a first analysis to quantify the seasonal variations in the prevalence of fronts and their associated velocity field.

3.1 Seasonal variability of submesoscale fronts

The dynamics of the horizontal flow can be expressed in terms of the strain tensor. This strain tensor can be decomposed into the vertical vorticity ζ, the horizontal

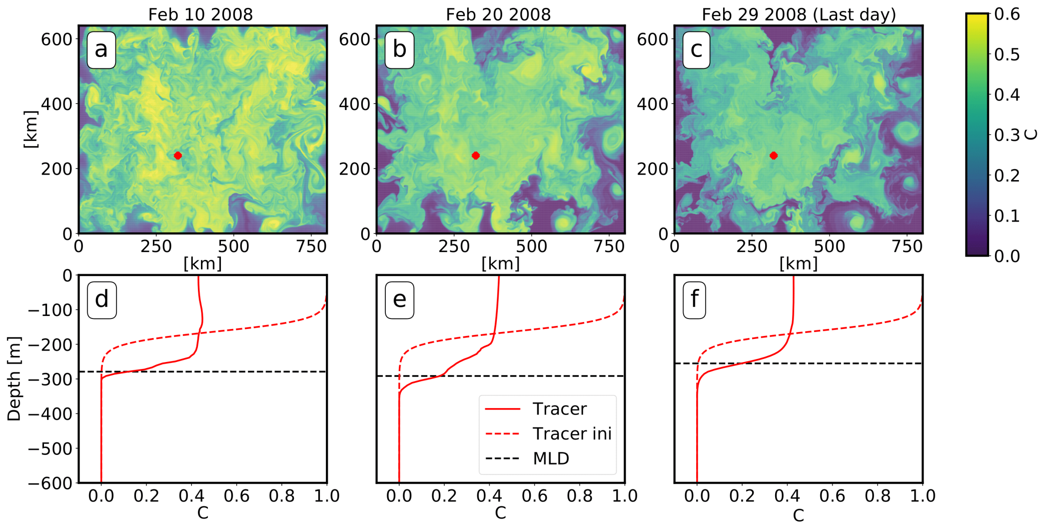

Figure 2. (a), (b) and (c) show the tracer concentration at the surface for February 10, 20 and 29. (d), (e) and (f) show the corresponding tracer vertical distribution (red line) at the location of the red dot. The dashed red line shows the initial vertical distribution of the tracer and the dashed black line is the MLD.

divergence δ and the strain rate σ (referred to as strain in the following for simplicity) as follows:

$$\zeta = \frac{\partial v}{\partial x} - \frac{\partial u}{\partial y} \quad ; \quad \delta = \frac{\partial u}{\partial x} + \frac{\partial v}{\partial y} \quad ; \quad \sigma = \sqrt{\left(\frac{\partial u}{\partial x} - \frac{\partial v}{\partial y}\right)^2 + \left(\frac{\partial u}{\partial y} + \frac{\partial v}{\partial x}\right)^2} \quad . \tag{3}$$

Strain and vorticity are often used to identify structures such as submesoscale fronts and eddies. Figure 1 displays the vorticity and strain within the domain on 8th February. During this winter period, we observe widespread and intense submesoscale structures, which are characterized by high vorticity and strain. This signature distinguishes them from eddy structures, which typically exhibit significant vorticity but weak strain patterns (Gula et al., 2014). Therefore, a flow decomposition based on joint probability density functions of surface vorticity and strain proves valuable for identifying fronts and eddies (Shcherbina et al., 2013). Previous studies have localized submesoscale fronts in vorticity-strain space as the regions near the lines $\sigma = |\zeta|$ (Shcherbina et al., 2013; McWilliams, 2016; Balwada et al., 2021). In a strongly ageostrophic regime ($|\delta| \sim |\zeta|$; Gula et al. (2014)), Barkan et al. (2019) demonstrated that fronts tend to cluster around the lines $\sigma = \sqrt{2}|\zeta|$. However, to our knowledge, none of the previous studies have precisely defined the area corresponding to submesoscale fronts. We have therefore chosen to define the frontal region by $\sigma > |\zeta|$ and with a restrictive criterion of $|\zeta/f| \sim Ro > 0.5$. The Ro criterion is based on the work of L. I. Siegelman (2020), who observed in a fine resolution model that submesoscale structures above the permanent thermocline characterised by ageostrophic flow are associated with $Ro > 0.5$. We define two subdomains, labelled 1A and 1C and delineated by dots and hatches, respectively, corresponding to the anticyclonic and cyclonic submesoscale fronts (Figure 4). The separation of cyclonic and anticyclonic fronts is useful because cyclonic fronts (1C) are known to contribute significantly to intense downward velocities, while anticyclonic fronts generally induce upwelling and weaker velocities (Gula, Taylor, et al., 2021). In addition, we name the two other zones dominated by vorticity based on Balwada et al. (2021): the anticy-

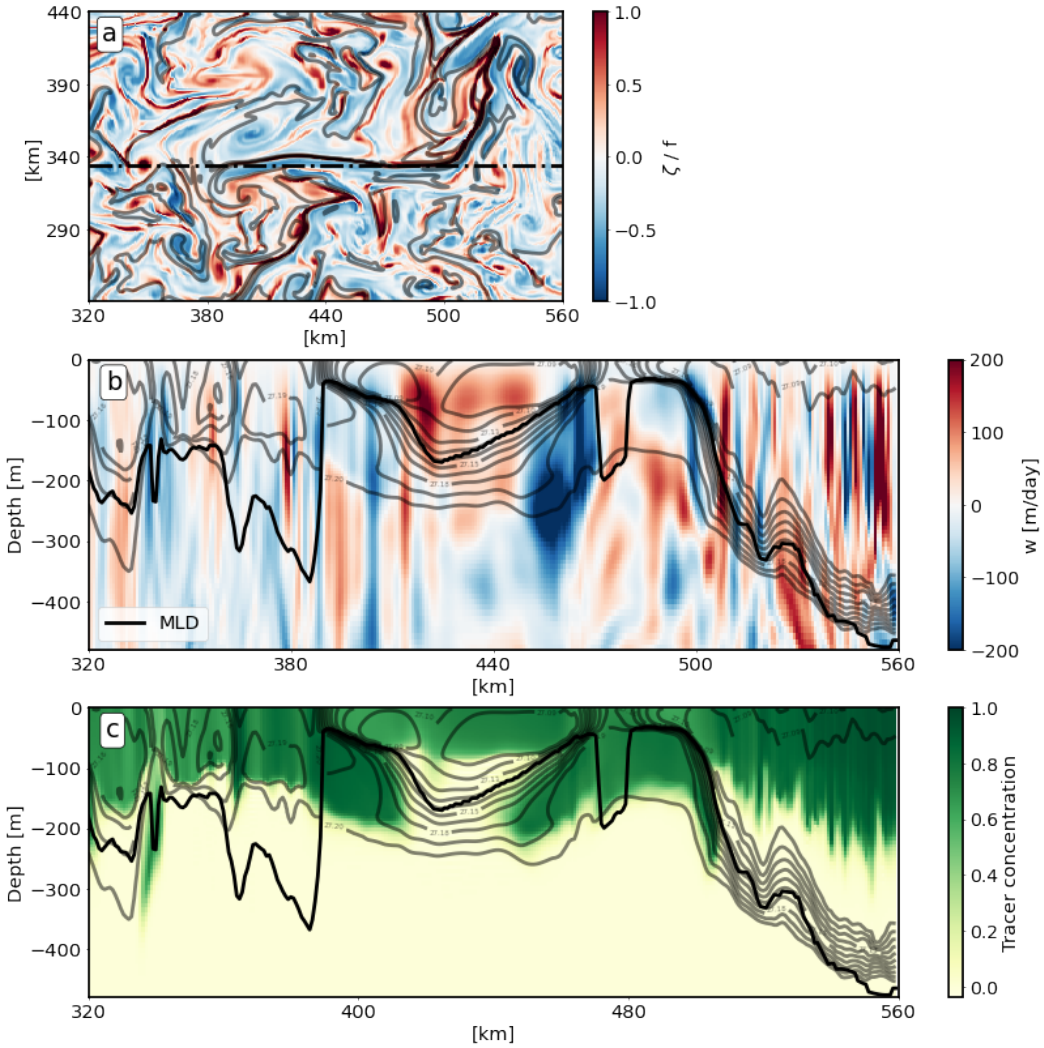

Figure 3. (a) Snapshot of the surface relative vorticity on the 3rd of April. The vertical section over a front is marked with a dashed black line. (b) Vertical cross section. The colors represent the vertical velocities. The black line is the MLD computed with a density threshold. The grey lines are the isopycnals. c) Tracer concentration on the same vertical section.

clonic zone (2) defined by $\zeta/f > 0$ and $\sigma < |\zeta|$, and the cyclonic zone, defined by $\zeta/f < 0$ and $\sigma < |\zeta|$. These regions correspond to areas within anticyclonic and cyclonic eddies.

Figure 4a displays the integrated surface strain-vorticity JPDF computed over March 2008. These statistics are computed within bins of size of 0.05×0.025 (vorticity $\times$ strain). The contour line delineates the region containing 99,99% of the grid points. A large fraction of the surface points exhibit weak vorticity and strain ($\zeta/f < 0.5$ and $\sigma/f < 0.5$), consistent with the quasi-geostrophic regime of turbulence expected to develop at this model resolution. The observed asymmetry, characterised by a peak in 1C, is the signature of submesoscale fronts (McWilliams, 2016; Buckingham et al., 2016). The 99.99% contour of the surface vorticity-strain JPDF is shown for each month in Figure 4b). Each season has a distinct JPDF signature, reflecting a clear shape evolution driven by the presence of submesoscale dynamics. The winter period exhibits the largest domain with

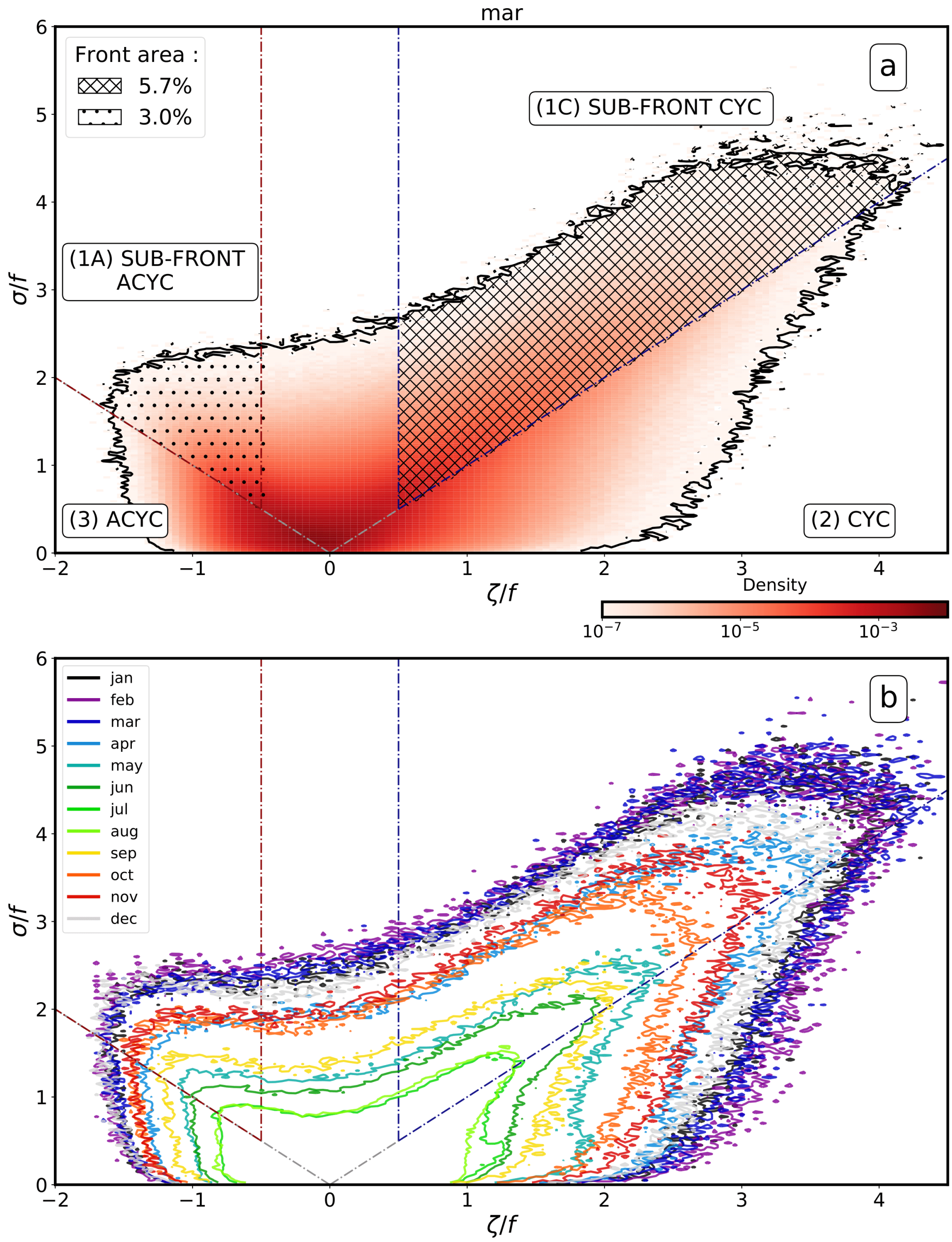

Figure 4. (a) Surface strain - vorticity JPDF in March. The black contour is the integrated domain containing 99.99% of the points. (1A) is the anticyclonic submesoscale frontal zone and (1C) is the cyclonic submesoscale frontal zone. (2) and (3) are the cyclonic and anticyclonic zones, respectively. The proportion of points within 1A (dotted area) and 1C (hatched area) are given. (b) Surface strain - vorticity JPDF domain contours (99.99% of the points) for each month.

the highest asymmetry due to more energetic submesoscales (Callies et al., 2015), while the JPDF envelope during the summer months is confined to a region of low strain and

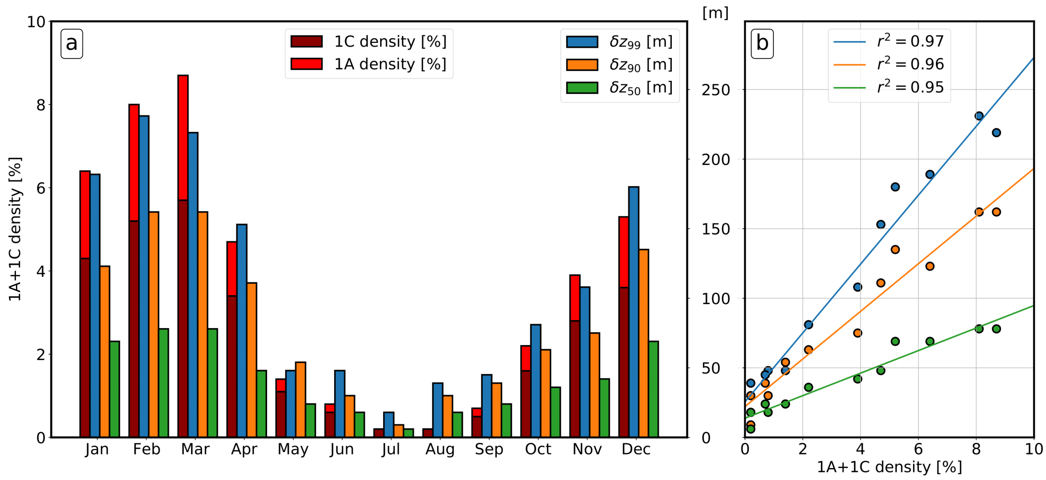

Figure 5. a) Deepening of the 50th (green), 90th (orange) and 99th (blue) tracer percentiles between the first and last day for each monthly experience. Red bars are the fraction of points within 1A and 1C. b) Linear regression between front density and tracer depth.

vorticity. Interestingly, the peak remains significant in spring, making this period particularly relevant for organic carbon export as the region hosts significant phytoplankton blooms in the euphotic layer. To quantitatively assess the presence of fronts, we calculate the fraction of points within regions 1A + 1C for each month, which we consider to be the front density (Figure 5a). The frontal area is maximum in March, accounting for about 9% of the total area (5.7 % in 1C). Conversely, the lowest fraction of submesoscales is found in July with less than 0.5%.

3.2 Seasonal variability of vertical velocity

Following the approach in Balwada et al. (2021), we look at the distribution of variables at depth as a function of surface vorticity and strain. This approach reveals interesting patterns in the vertical velocity w. For each month, we computed the distribution of the bin-averaged vertical velocity $\langle w_z \rangle$, conditioned on surface vorticity and strain over 20 vertical z levels equally spaced from the surface to 2×MLD. An example for March is shown in Figure 6. Similar to the density JPDF, we use 3-hourly outputs (averages) during the first 29 days of each month. Our approach is similar to that of Balwada et al. (2021), with a key difference being that instead of considering a horizontally constant MLD, we compute the MLD at each grid point and for each time step.

The cyclonic part is generally associated with $\langle w \rangle < 0$. The largest negative velocities are within the 1C area and persist down to depths of $2\times MLD$. For the anticyclonic area, $\langle w \rangle$ is generally positive near the surface, regardless of fronts or eddies. However, some observations change below the MLD. First, the velocities inside the eddy area ($|\zeta| > |\sigma|$) become much weaker, while the velocities inside the frontal area remain significant. We also observe a shift in the sign of the velocities in 1A close to the MLD and below. This shift is a direct consequence of the methodological limitation. Indeed, the dynamics conditioned at depth, especially below the MLD, may not always be directly linked to surface properties. First, the fronts are often surface intensified and the associated second circulation may not extend to the MLD and below. In addition, vertical velocities induced by a front often follow isopycnal paths that are not vertical and include a horizontal component (Freilich & Mahadevan, 2021). Consequently, the associated subduction may not necessarily be located directly beneath its apparent surface signature, and lateral advection transport may also be induced. This is particularly problematic for the light anticyclonic side of fronts, whose upward path may be above the dense cyclonic downward path (Figure A1). Consequently, below a certain depth, we associate part of the cyclonic downward velocity with the 1A area, biasing the results, especially for months associated with deep MLDs such as March.

Focusing on the frontal areas, we compare the vertical profiles of vertical velocity for each month. We compute the density-weighted mean $\langle w \rangle$ (i.e. the mean velocities weighted by the corresponding bin density) for 1C and 1A over the vertical (Figure 7a,b). The maximum velocities within the fronts are typically observed at depths corresponding to 0.3-0.4 × MLD, and usually drop to a much weaker value near the MLD. Region 1C is consistently associated with downwelling, with varying seasonal intensities ranging from -130 m/day (winter) to -10 m/day (summer). In contrast, region 1A shows upwelling with values ranging from 5 m/day to 70 m/day. Below the MLD, $\langle w \rangle$ remains consistently negative in 1C, while in 1A, $\langle w \rangle$ can change sign below $1.1 \times MLD$. We observe such a transition from positive to negative values below $1.1 \times MLD$ from October to March, which are months associated with deep MLDs, presumably due to the bias mentioned above.

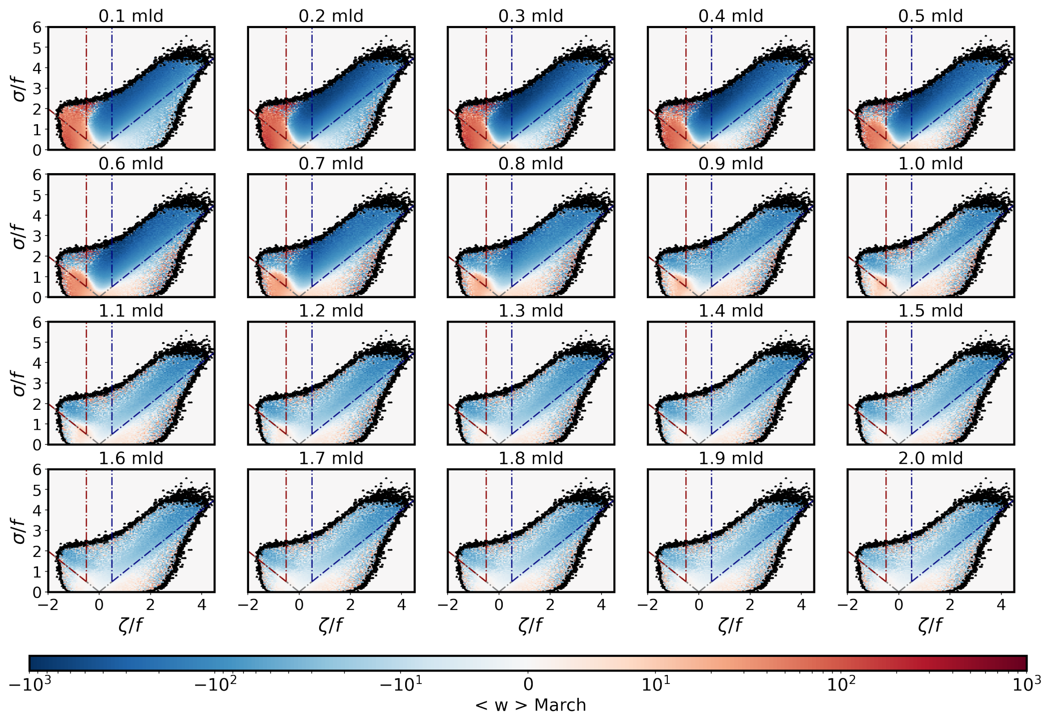

Figure 6. Bin-averaged vertical velocity conditionned on surface vorticity and strain at different vertical levels during March. The black contour is the integrated domain containing 99.99% of the points. The remaining 0.01% of points are hidden.

To analyse subduction, we focus in particular on the mean vertical velocity at the MLD $\langle w_{mld} \rangle$ Figure 8. Although there is a monthly variability in the distribution of $\langle w_{mld} \rangle$, we still observe a consistent pattern in the vertical velocity. Notably, both anticyclonic (3) and cyclonic (2) features are associated with positive vertical velocities. Cyclonic fronts in region 1C exhibit strong downward velocities, while anticyclonic fronts in region 1A exhibit a mixture of positive and negative vertical velocities. Most of the area of region 1A in strain-vorticity space has negative vertical velocities, but the area mean is still positive (Figure 7b) due to the much higher density of points in the lower strain and vorticity region associated with positive vertical velocities. However, with the exception of the 1A area, we observe robust w patterns constrained by surface dynamical features, independent of season and depth. These observations support our hypothesis that the surface dynamics are strongly linked to the vertical velocity at the MLD.

The mean vertical velocity also appears to follow a seasonal pattern. The relationship between the frontal area density and $\langle w_{mld} \rangle$ in 1A and 1C is shown in Figure 7c,d. It shows a moderate correlation with $r^2 = 0.37$ in 1C and $r^2 = 0.54$ in 1A (Taylor, 1990; Ratner, 2009), which suggests that vertical velocities are more intense at the MLD when front density is higher.

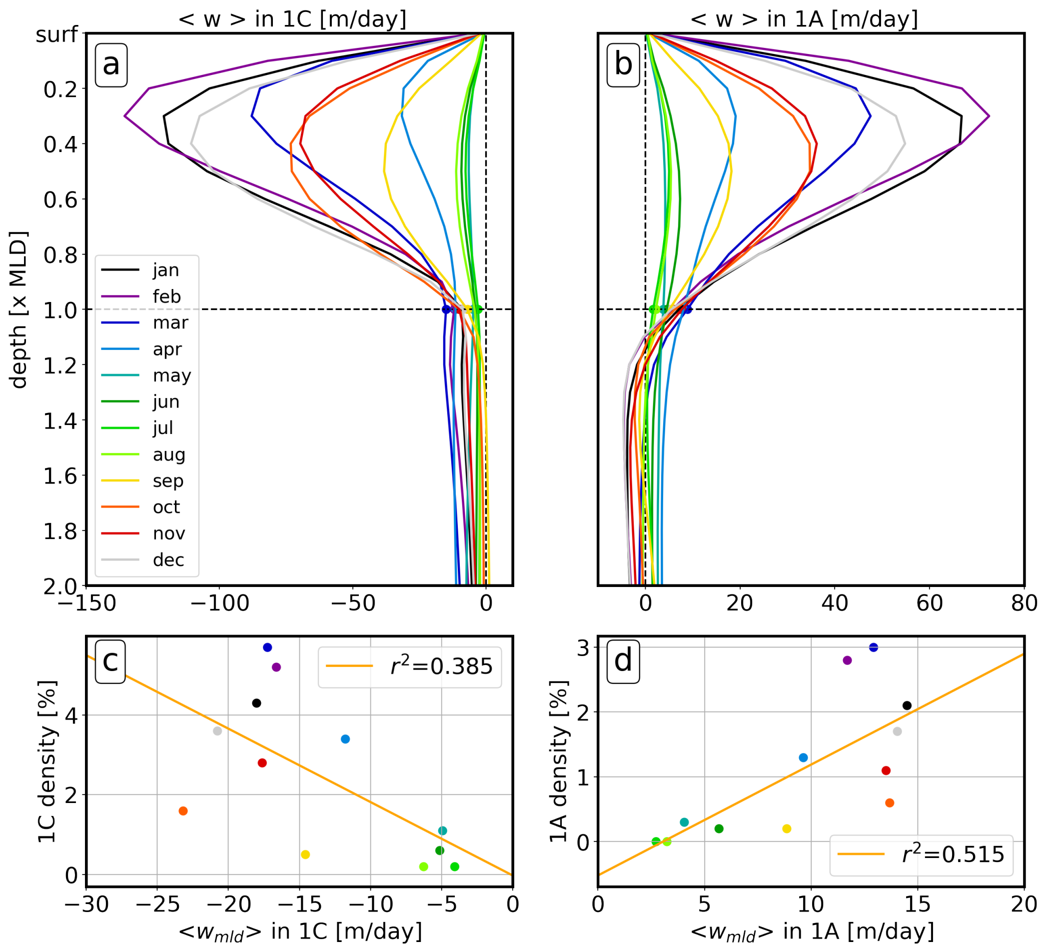

Figure 7. Mean vertical velocity $\langle w \rangle$ in 1A (a) and 1C (b) between the surface and 2 * MLD for each month. Linear regression between the mean velocity at MLD $\langle w_{mld} \rangle$ and the front density in 1A and 1C.

4 The seasonal tracer evolution

In this section we analyse the tracer transport at depth, focusing in particular on the vertical advective subduction that occurs within fronts.

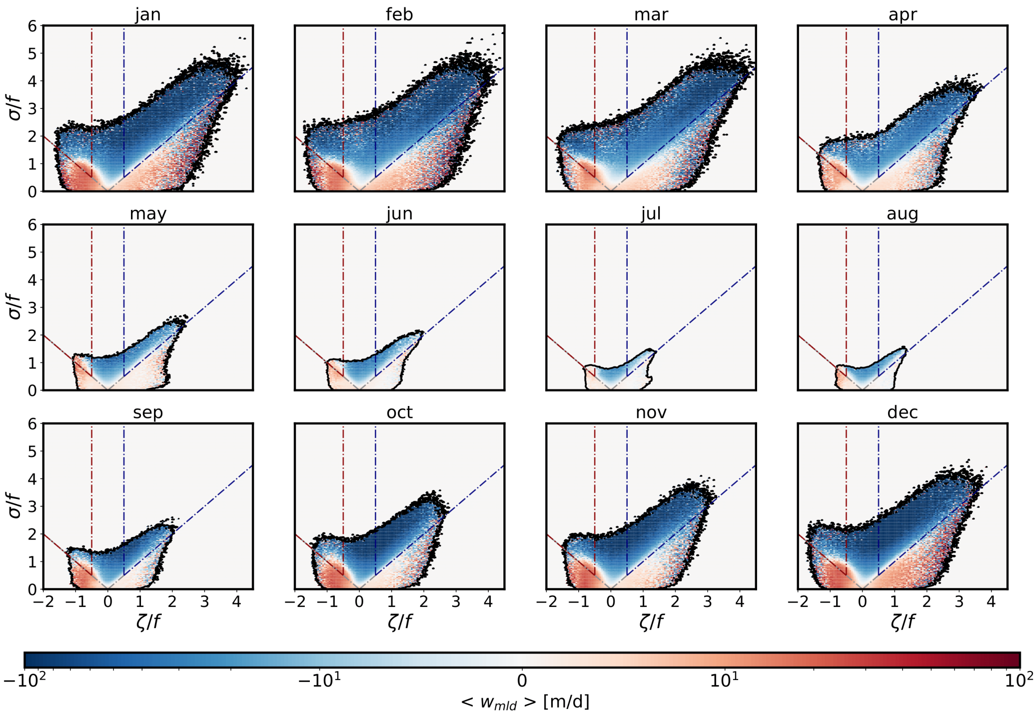

Figure 8. Surface strain-vorticity JPDF conditioned with the mean vertical velocity w at MLD and for each month. Black contour is the integrated domain that contain 99.99% of points (points outside have been removed).

4.1 Tracer deepening

We examine the tracer evolution over the vertical in Figure 9, which displays the average tracer concentration within 3-meter bins and the spatially averaged evolution of the mixed layer depth $\langle MLD \rangle$. Over the study period, the ML has a typical seasonal evolution characterised by a stable and large depth in winter, intense stratification in spring, a shallow and stable depth in summer and a gradual deepening in fall. To better estimate the evolution of the tracer, we compute the distribution of the tracer concentration as a function of depth and monitor the distribution's median, 90th, and 99th percentiles. Each month the tracer spreads deeper into the water column, and the concentration within the ML decreases. It is important to note that since the simulation has open boundaries, the tracer can escape through the boundaries, but this does not affect the statistical results. The tracer depth is particularly important for carbon export, as the carbon sequestration time is directly dependent on the depth of injection (Bol et al., 2018). The difference between the depth of each percentile on the first day and on the last day ($\delta z_{99}, \delta z_{90}, \delta z_{50}$) is plotted in Figure 5a. The varying seasonal conditions allowed us to compute the linear regression between the front density and the tracer deepening. Interestingly, δz_{99},δz_{90} and δz_{50} appear to be significantly correlated with the front density (Figure 5b). This suggests that the front density may impact the depth at which the tracer is subducted. Consequently, the surface conditions can potentially be used as an indicator to estimate the redistribution of tracer at depth in this region.

4.2 Seasonal tracer subduction driven by submesoscale fronts

To estimate the contribution of submesoscale fronts to tracer vertical transport, we mapped the vertical transport of the tracer, (wC), in surface strain-vorticity space

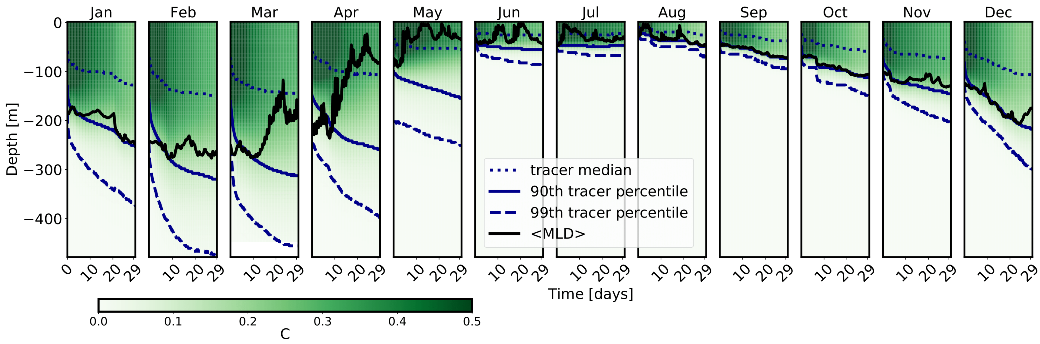

Figure 9. Tracer distribution and evolution for each month. The tracer concentration is vertically averaged over 3-meter bins. The black line is the spatial mean of the mixed layer depth computed for each time step (3h) with a density threshold. Blue lines represent the 50th (dotted), 90th (solid) and 99th (dashed) percentiles of the tracer.

– w represents the vertical velocity, and C is the tracer concentration. We computed the sum ΣwC within each bin and, similar to part 3.3, these results are computed for 20 vertical levels between the surface and z = 2 × MLD. An example for March is given in Figure 10. Inside the mixed layer, the vertical transport is similar to what we observe with velocity (Figure 6). This is because the tracer is almost uniform across the mixed layer and always positive. Therefore, the total transport is directly related to the mean velocity. Below the MLD, however, the transport is mostly negative in each region. This is because no tracer was injected at this depth during the initial conditions. A small part in the eddy region still shows positive transport, suggesting that some of the subducted tracer may be reinjected into the mixed layer. The blue contours indicate the region contributing to 50% and 99% of the downward transport. It is clear that most of the downward contribution is associated with low strain and vorticity, where the density is maximum 4. However, the 1C area also appears to be a region that contributes significantly to the export.

To confirm this trend, for each month and within the depth range between the surface and 2 × MLD, we calculated the total tracer fluxes inside 1A and 1C, i.e., the sum of the bins in 1A and 1C (Figures 11a and b). We also estimated the fraction of these fluxes relative to the total downward fluxes, i.e., $\frac{\Sigma wC_{1C}}{\Sigma wC_{wC<0}}$ and $\frac{\Sigma wC_{1A}}{\Sigma wC_{wC<0}}$ (Figures 11c and d). Similar to w, the transport wC in 1C and 1A reaches a peak at z = 0.3-0.4 MLD and decreases significantly near the MLD. In 1C, the transport remains always negative and can contribute significantly to the total downward transport between the surface and $2 \times MLD$. In 1A, however, the transport shifts from positive to negative precisely at the MLD. It is difficult to interpret the results in 1A below the MLD. As no tracer was injected below the MLD, no significant positive contribution can be observed. In addition, the negative export in this region may also also due to the bias mentioned in section 3.2.

Focusing on subduction, we plotted $w_{mld}C_{mld}$ conditioned on vorticity and strain for each month in Figure 12. Irrespective of the season, the anticyclonic (3) and cyclonic (2) areas contribute mainly to the upward transport, while the remaining region is associated with mainly downward transport. Again, we observe the important contribution of the 1C area, which participates mainly in the downward fluxes. The positive transport near the anticyclonic eddy boundary and the negative transport for intense strain in 1A seem to compensate each other as suggested by Figure 11 b).

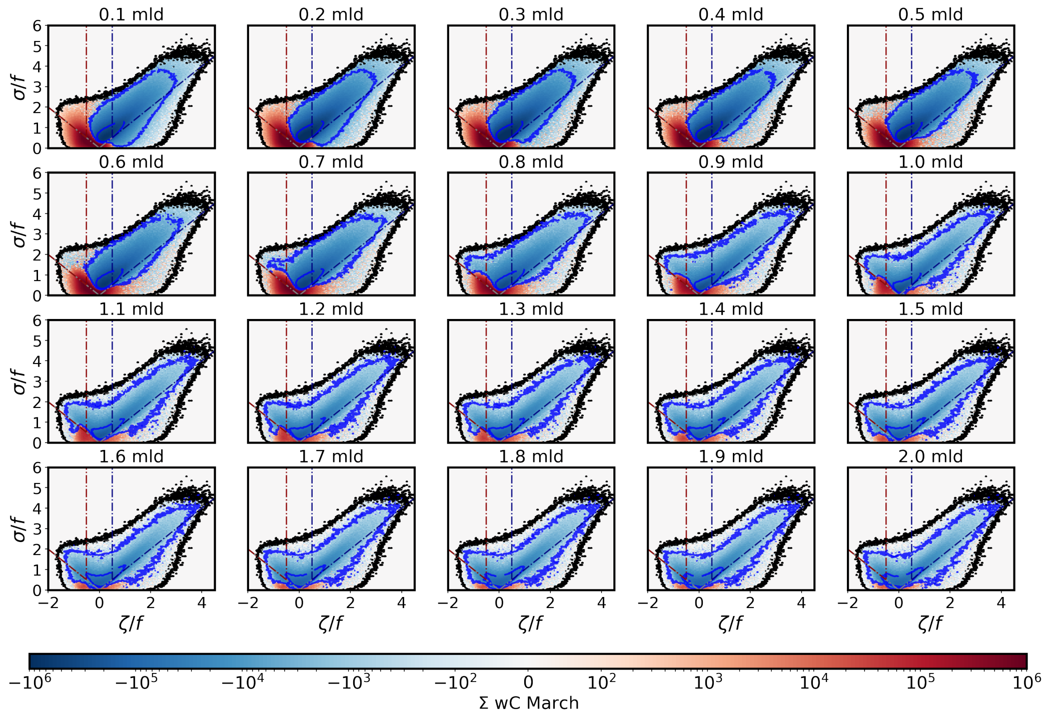

Figure 10. Surface strain-vorticity JPDF conditioned with the sum of vertical transport ΣwC at different vertical levels for March. Black contour is the integrated domain containing 99.99% of the points. Points outside have been removed. Blue contours include the integrated points contributing to 50% (inside) and 99% (outside) of the total downward transport.

We observe a singularity at the MLD in Figures 11c,d. This is due to the total downward fluxes (not shown), which have a local extremum at this depth. At present, this maximum is not fully understood. We therefore focus on the two depths 0.9 MLD and 1.1 MLD to obtain a more robust description. As mentioned above, in 1A we observe a shift in the sign of ΣwC , from positive (i.e. obduction) to negative (i.e. subduction). Overall, the net fluxes near the MLD are close to 0, indicating that 1A does not contribute significantly to subduction, the absolute contribution being 1-5%. Conversely, the fluxes associated with 1C at the MLD are important and represent a significant contribution in terms of subduction, particularly during the winter and spring months, with a contribution of 30-40% of the total flux. There is a slight decrease in the contribution with depth, which again could be due to the limitation of the methodology. We find the evidence of a clear relationship between the tracer fluxes, the subduction contribution around the MLD, and the front density (Figures 11e-h). In particular, the subduction contribution in 1C shows a direct correlation with the front density ($r^2 = 0.90-0.92$). The linear relationship is also observed for the anticyclonic front, but not as effective ($r^2 = 0.66-0.74$). This results suggests that, in this region, the frontal contribution and associated flux can be estimated from the surface strain-vorticity front signature.

5 Discussion

5.1 Bias and futur improvements

Few studies have used surface strain-vorticity statistical tools to characterise submesoscale dynamics in both observations and models (Shcherbina et al., 2013; Rocha et

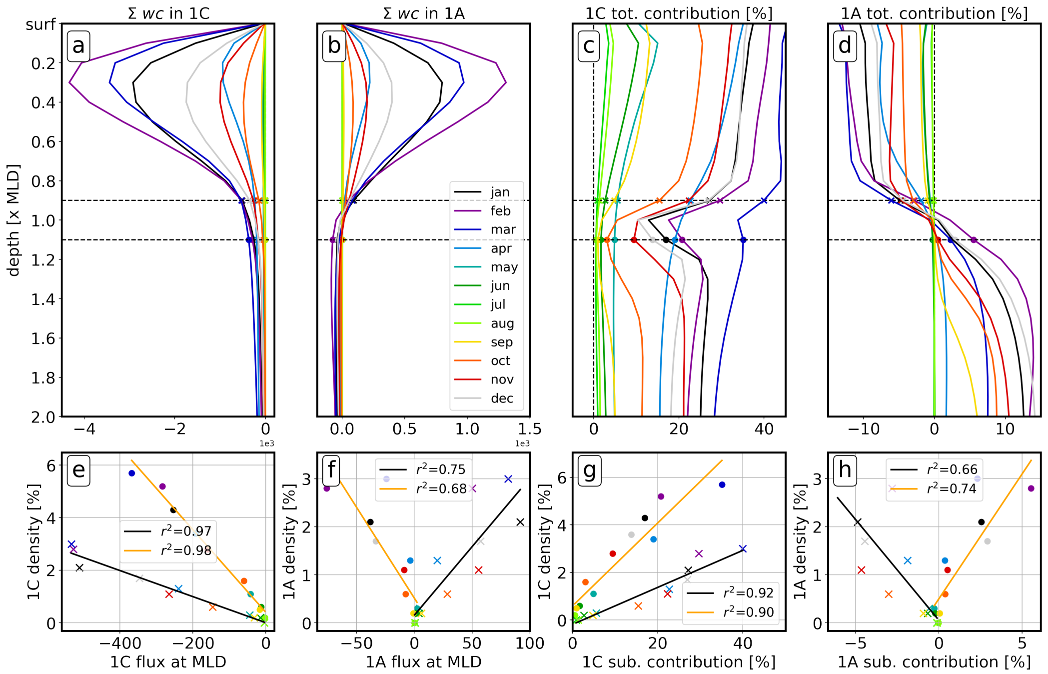

Figure 11. Net fluxes in 1C (a) and 1A (b) between surface and 2 * MDL. Total negative flux contribution for 1C (c) and 1A (d). Corresponding linear regressions between frontal area and fluxes at MLD / total subduction contribution are given for 1C (e,g) and 1A (f,h).

al., 2016; Balwada et al., 2021; Vic et al., 2022; Wang et al., 2022). To our knowledge, Balwada et al. (2021) is the only study using JPDFs and tracer vertical transport conditioned on surface strain and vorticity to estimate the submesocale frontal contribution at depth. As mentionned in Balwada et al. (2021), it is important to note that results from numerical simulations can be highly sensitive to the grid resolution, but also the output frequency (Figure B1). Due to numerical storage constraints, we chose here to use 3-h averaged outputs, but it is worth noting that these outputs slightly smoothed the frontal impact compared to hourly snapshots, resulting in a 0.5% loss in density. Therefore, our results may underestimate the effecs of the front on tracer transport.

One important limitation of this method is the connection between the surface dynamics and the dynamics at depth, as mentioned in section 3.2. In particular, the vertical velocities induced by a front are limited in depth and do not always follow a 1D vertical direction. Furthermore, the vertical structure of the fronts can be more complex and is not always surface intensified, as discussed in Wang et al. (2022). These limitations result in a bias that may be depth dependent and needs to be properly quantified in order to better understand the limited zone where such a method can be applied. This implies that the frontal isopycnal paths need to be accurately determined, which is a challenging task that remains to be addressed.

Finally, the definitions of the submesoscale frontal regions 1A and 1C used here are based on simplified assumptions. While these definitions provide reasonable approximations for estimating the initial impact of submesoscale fronts, they require further refinement. In reality, the definition of a submesoscale frontal region is more complex and may depend on the dynamics itself. Buckingham et al. (2016) demonstrated that ζ values in submesoscale regions are influenced by the Coriolis frequency and by the ratio of lateral to vertical buoyancy gradients. The Ro criteria used in our study may not be fully ap-

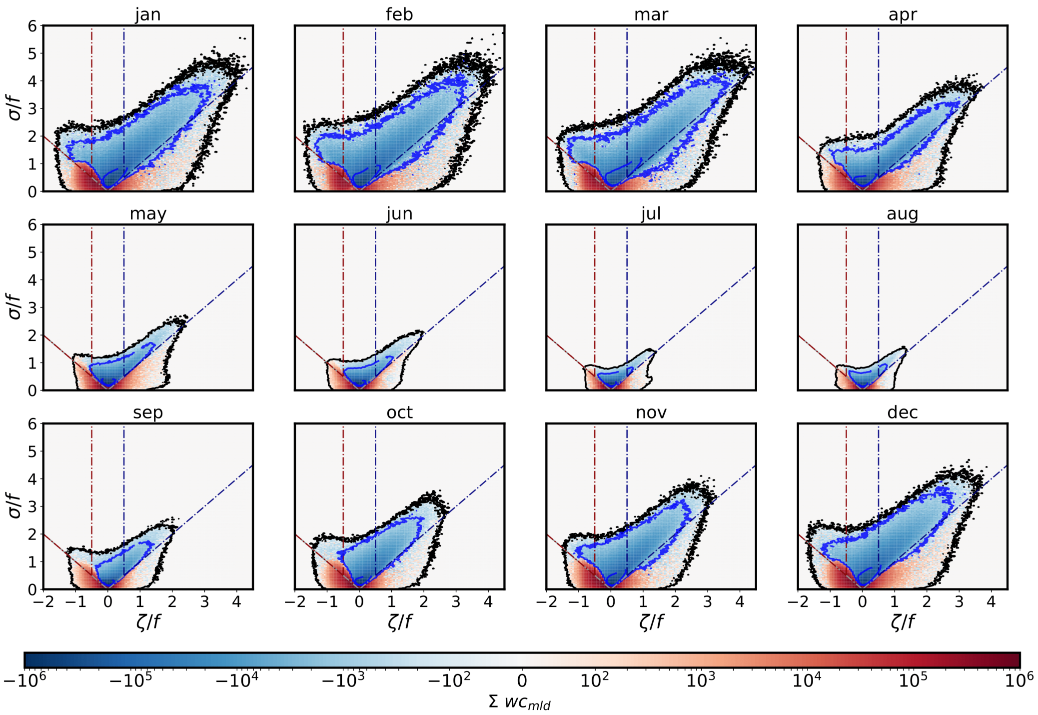

Figure 12. The sum of vertical advection $\Sigma w_{mld} \cdot C_{mld}$ conditioned by surface vorticity and strain. Integrated blue contours indicate 99% and 50% of the total negative flux. The black contour contains 99.99% of the points (points outside have been hidden).

propriate in certain regions, such as the Gulf Stream, where Ro is about 0.7–1.0 at the submesoscale, exceeding the values in our region. Therefore, we highlight the need for further theoretical development to precisely define a submesoscale zone within the surface strain-vorticity space. This will be crucial in the future for accurate estimation of tracer export influenced by submesoscale dynamics.

However, compared to previous studies, we observe similar associations between surface properties and transport at the MLD, and we also find similar orders of magnitude in terms of submesoscale contributions, reinforcing our confidence in the results.

5.2 Towards a better parameterization of the effect of fronts on tracer subduction

The main objective of this study was to gain a better understanding of the contribution of fronts to water subduction in a seasonal perspective. Proper quantification of subduction is crucial for understanding complex ocean mechanisms such as the carbon pump and heat transfer. Our seasonal study has allowed us to clearly identify front signatures and evaluate their impact on the transport of upper layer water to depth. Significant variations in front density allow us to infer a parameterization of the impact of fronts on tracer transport based solely on their surface characteristics. An important result is that the vertical advective subduction contribution can be estimated directly from the surface dynamics. So far, satellites have not been able to detect submesoscale features (Ballarotta et al., 2019). However, with the ongoing Surface Water and Ocean Topography (SWOT) mission (Fu & Ubelmann, 2014), it will soon be possible to improve the altimetry resolution to 10-30 km. This will allow better determination of front density and associated subduction rates, which is particularly relevant for biogeochemical studies focusing on the contribution of submesoscale features to the biological carbon pump, often referred to as the eddy-subduction pump (Boyd et al., 2019). Submesoscale processes capable of injecting particles to depth have not been clearly quantified yet, and this may partly explain why the carbon demand of the mesopelagic ecosystem exceeds the downward flux of presumably sinking POC by a factor of 2-3 (Burd et al., 2010). While this study used a simplified approach with homogenized tracer initialization within the ML, the same methodology could be adapted to study the front's contribution to carbon export and nutrient injection using coupled biochemical modeling. In addition, it is important to note that the seasonal results presented here are based on one year of data, and inter-annual variability can be significant (Berta et al., 2020). Further studies are needed to assess the sensitivity associated with different time periods, regions, and numerical models.

6 Conclusion

The present study investigates the seasonal fate of a passive tracer released monthly in the surface mixed layer using a realistic high-resolution simulation in the North Atlantic. Using surface strain and vorticity criteria, we identified and quantified the areas occupied by fronts and the density of frontsfor each month in 2008. Our observations revealed a deep sinking of the tracer in the presence of submesoscale activity and a consistent correlation between front density and tracer sinking emerged, independent of the mixed layer depth evolution. Remarkably, our investigation revealed that cyclonic submesoscale fronts, ranging from 0.5% in summer to about 6% in winter, contribute significantly to the total vertical advective subduction, ranging from 0.5% to 40%, respectively. These results not only confirm the efficacy of using surface vorticity-strain criteria for front analysis, but also emphasize the need to study fronts from a seasonal perspective.

Appendix A Front scheme

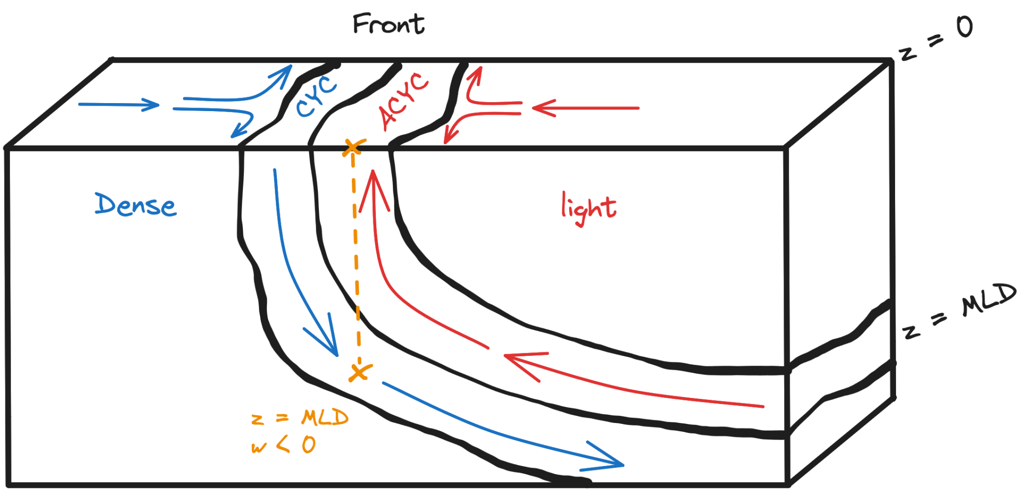

Figure A1. Scheme of a front cross-section. The orange cross represents the observation point. In this particular case, the vertical velocity below the surface anticyclonic front is not associated with an upwelling at z=MLD due to the slope of the front. This leads to a bias in our statistical results around and below the MLD.

Appendix B Time-averaged outputs sensibility

We have compared the JPDF and the 1C density during the first 5 days of March with different output frequencies. The figure B1 shows a significant difference between daily-averaged (1.6% of cyclonic front density) and hourly averaged or snapshot outputs ($>5\%$ of cyclonic front density).

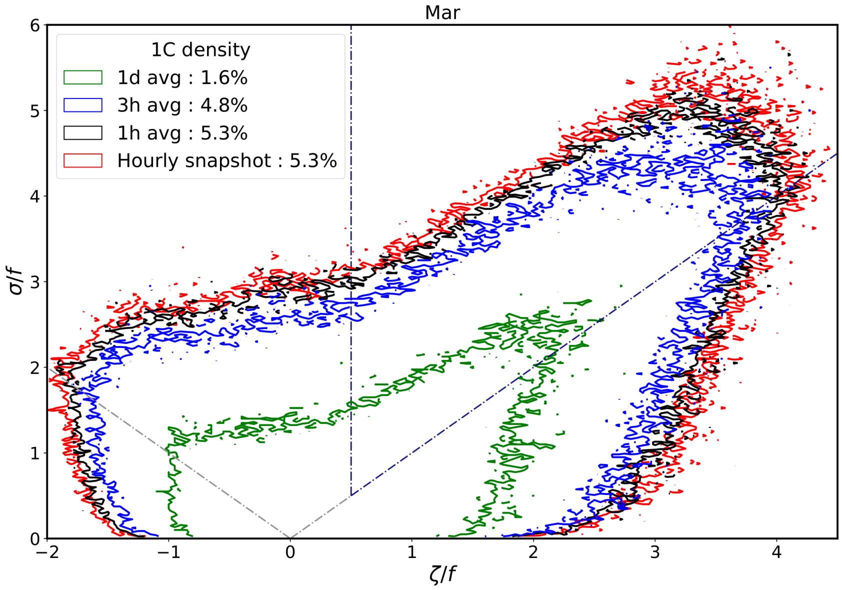

Figure B1. Surface strain-vorticity JPDF for 4 different output types which are daily averaged (green), 3-hour averaged (blue), 1-hour averaged (black) and hourly snapshot (red). The black contour is the integrated domain containing 99.99% of the points. The fraction of points within 1C is computed for each JPDF.

Acknowledgments

T.P. received a Ph.D. grant from École Normale Superieure Paris-Saclay. This work was also supported by the ISblue project, an Interdisciplinary graduate school for the blue planet (ANR-17-EURE-0015), and co-funded by a grant from the French government under the program "Investissements d'Avenir". J.G. would like to acknowledge support from the French National Agency for Research (ANR) through the project DEEPER (ANR-19-CE01-0002-01). Simulations were performed using HPC resources from GENCI-TGCC (Grants 2022-A0090112051), and from HPC facilities DATARMOR of "Pôle de Calcul Intensif pour la Mer" at Ifremer Brest France.

References

Ballarotta, M., Ubelmann, C., Pujol, M. I., Taburet, G., Fournier, F., Legeais, J. F., ... Picot, N. (2019, aug). On the resolutions of ocean altimetry maps. *Ocean Science*, *15*(4), 1091–1109. doi: 10.5194/os-15-1091-2019

Balwada, D., Smith, K. S., & Abernathey, R. (2018, sep). Submesoscale Vertical Velocities Enhance Tracer Subduction in an Idealized Antarctic Circumpolar Current. *Geophysical Research Letters*, *45*(18), 9790–9802. Retrieved from `https://agupubs.onlinelibrary.wiley.com/doi/10.1029/2018GL079244` doi: 10.1029/2018GL079244

Balwada, D., Xiao, Q., Smith, S., Abernathey, R., & Gray, A. R. (2021, jun). Vertical fluxes conditioned on vorticity and strain reveal submesoscale ventilation. *Journal of Physical Oceanography*. doi: 10.1175/jpo-d-21-0016.1

Barkan, R., Molemaker, M. J., Srinivasan, K., McWilliams, J. C., & D'asaro, E. A. (2019, jun). The role of horizontal divergence in submesoscale frontogenesis. *Journal of Physical Oceanography*, *49*(6), 1593–1618. doi: 10.1175/JPO-D-18-0162.1

Berta, M., Griffa, A., Haza, A. C., Horstmann, J., Huntley, H. S., Ibrahim, R., ... Poje, A. C. (2020, oct). Submesoscale Kinematic Properties in Summer and Winter Surface Flows in the Northern Gulf of Mexico. *Journal of Geophysical Research: Oceans*, *125*(10), e2020JC016085. Retrieved from https://agupubs.onlinelibrary.wiley.com/doi/10.1029/2020JC016085 doi: 10.1029/2020JC016085

Bol, R., Henson, S. A., Rumyantseva, A., & Briggs, N. (2018, dec). High-Frequency Variability of Small-Particle Carbon Export Flux in the Northeast Atlantic. *Global Biogeochemical Cycles*, *32*(12), 1803–1814. doi: 10.1029/2018GB005963

Bopp, L., Resplandy, L., Orr, J. C., Doney, S. C., Dunne, J. P., Gehlen, M., ... Vichi, M. (2013). Multiple stressors of ocean ecosystems in the 21st century: Projections with CMIP5 models. *Biogeosciences*, *10*(10), 6225–6245. doi: 10.5194/bg-10-6225-2013

Boyd, P. W., Claustre, H., Levy, M., Siegel, D. A., & Weber, T. (2019). Multi-faceted particle pumps drive carbon sequestration in the ocean. *Nature*, *568*(7752), 327–335. doi: 10.1038/s41586-019-1098-2

Buckingham, C. E., Naveira Garabato, A. C., Thompson, A. F., Brannigan, L., Lazar, A., Marshall, D. P., ... Belcher, S. E. (2016). Seasonality of submesoscale flows in the ocean surface boundary layer. *Geophysical Research Letters*, *43*(5), 2118–2126. doi: 10.1002/2016GL068009

Burd, A. B., Hansell, D. A., Steinberg, D. K., Anderson, T. R., Arístegui, J., Baltar, F., ... Tanaka, T. (2010, aug). Assessing the apparent imbalance between geochemical and biochemical indicators of meso- and bathypelagic biological activity: What the @$! is wrong with present calculations of carbon budgets? *Deep-Sea Research Part II: Topical Studies in Oceanography*, *57*(16), 1557–1571. doi: 10.1016/j.dsr2.2010.02.022

Callies, J., Ferrari, R., Klymak, J. M., & Gula, J. (2015). Seasonality in submesoscale turbulence. *Nature Communications*, *6*(1), 6862. Retrieved from https://doi.org/10.1038/ncomms7862 doi: 10.1038/ncomms7862

Cao, H., & Jing, Z. (2022, feb). Submesoscale ageostrophic motions within and below the mixed layer of the northwestern Pacific Ocean. *Journal of Geophysical Research: Oceans*. Retrieved from https://onlinelibrary.wiley.com/doi/10.1029/2021JC017812 doi: 10.1029/2021JC017812

Capet, X., Campos, E. J., & Paiva, A. M. (2008, aug). Submesoscale activity over the Argentinian shelf. *Geophysical Research Letters*, *35*(15), L15605. Retrieved from http://doi.wiley.com/10.1029/2008GL034736 doi: 10.1029/2008GL034736

Chelton, D. B., Schlax, M. G., & Samelson, R. M. (2011, oct). Global observations of nonlinear mesoscale eddies. *Progress in Oceanography*, *91*(2), 167–216. doi: 10.1016/j.pocean.2011.01.002

de Boyer Montégut, C., Madec, G., Fischer, A. S., Lazar, A., & Iudicone, D. (2004, dec). Mixed layer depth over the global ocean: An examination of profile data and a profile-based climatology. *Journal of Geophysical Research*, *109*(C12), C12003. Retrieved from http://doi.wiley.com/10.1029/2004JC002378 doi: 10.1029/2004JC002378

Fox-Kemper, B., Adcroft, A., Böning, C. W., Chassignet, E. P., Curchitser, E., Danabasoglu, G., ... Yeager, S. G. (2019, feb). *Challenges and prospects* *in ocean circulation models* (Vol. 6) (No. FEB). Frontiers Media S.A. doi: 10.3389/fmars.2019.00065

Freilich, M., & Mahadevan, A. (2021, may). Coherent Pathways for Subduction From the Surface Mixed Layer at Ocean Fronts. *Journal of Geophysical Research: Oceans*, *126*(5), e2020JC017042. Retrieved from https://onlinelibrary.wiley.com/doi/10.1029/2020JC017042 doi: 10.1029/2020JC017042

Fu, L. L., & Ubelmann, C. (2014, feb). On the transition from profile altimeter to swath altimeter for observing global ocean surface topography. *Journal of Atmospheric and Oceanic Technology*, *31*(2), 560–568. doi: 10.1175/JTECH-D-13-00109.1

Gula, J., Molemaker, J. J., & Mcwilliams, J. C. (2014). Submesoscale cold filaments in the Gulf Stream. *Journal of Physical Oceanography*, *44*(10), 2617–2643. doi: 10.1175/JPO-D-14-0029.1

Gula, J., Taylor, J., Shcherbina, A., & Mahadevan, A. (2021, jan). Submesoscale processes and mixing. In *Ocean mixing: Drivers, mechanisms and impacts* (pp. 181–214). Elsevier. doi: 10.1016/B978-0-12-821512-8.00015-3

Gula, J., Theetten, S., Cambon, G., & Roullet, G. (2021, June). *Description of the gigatl simulations.* Zenodo. Retrieved from https://doi.org/10.5281/zenodo.4948523 doi: 10.5281/zenodo.4948523

J. J. Becker D. T. Sandwell, W. H. F. S. J. B. B. B. J. D. D. F. J. F. S. I. S.-H. K. R. L. K. M. S. N. A. P. R. T. J. V. R. G. W., & Weatherall, P. (2009). Global Bathymetry and Elevation Data at 30 Arc Seconds Resolution: SRTM30_PLUS. *Marine Geodesy*, *32*(4), 355–371. Retrieved from https://doi.org/10.1080/01490410903297766 doi: 10.1080/01490410903297766

Klein, P., & Lapeyre, G. (2009). *The oceanic vertical pump induced by mesoscale and submesoscale turbulence* (Vol. 1). doi: 10.1146/annurev.marine.010908.163704

Lacour, L., Briggs, N., Claustre, H., Ardyna, M., & Dall'Olmo, G. (2019, mar). The Intraseasonal Dynamics of the Mixed Layer Pump in the Subpolar North Atlantic Ocean: A Biogeochemical-Argo Float Approach. *Global Biogeochemical Cycles*, *33*(3), 266–281. doi: 10.1029/2018GB005997

Lapeyre Guillaume, K. P. (2006). *Impact of the small-scale elongated filaments on the oceanic vertical pump* (Vol. 64) (Article No. 6). FRANCE. Retrieved from https://archimer.ifremer.fr/doc/00000/2459/ doi: https://doi.org/10.1357/002224006779698369

Large, W. G., McWilliams, J. C., & Doney, S. C. (1994, nov). Oceanic vertical mixing: A review and a model with a nonlocal boundary layer parameterization. *Reviews of Geophysics*, *32*(4), 363. Retrieved from http://doi.wiley.com/10.1029/94RG01872 doi: 10.1029/94RG01872

Le Corre, M., Gula, J., & Tréguier, A. M. (2020, apr). Barotropic vorticity balance of the North Atlantic subpolar gyre in an eddy-resolving model. *Ocean Science*, *16*(2), 451–468. doi: 10.5194/os-16-451-2020

Lévy, M., Couespel, D., Haëck, C., Keerthi, M., Mangolte, I., & Prend, C. J. (2024). The Impact of Fine-Scale Currents on Biogeochemical Cycles in a Changing Ocean. *Annual Review of Marine Science*, *16*(1), 1–25. doi: 10.1146/annurev-marine-020723-020531

Lévy, M., Franks, P. J., & Smith, K. S. (2018, dec). *The role of submesoscale currents in structuring marine ecosystems* (Vol. 9) (No. 1). Nature Publishing Group. doi: 10.1038/s41467-018-07059-3

Llort, J., Langlais, C., Matear, R., Moreau, S., Lenton, A., & Strutton, P. G. (2018). Evaluating Southern Ocean Carbon Eddy-Pump From Biogeochemical-Argo Floats. *Journal of Geophysical Research: Oceans*, *123*(2), 971–984. doi: 10.1002/2017JC012861

Mahadevan, A. (2016, jan). The Impact of Submesoscale Physics on Primary

Productivity of Plankton. *Annual Review of Marine Science*, *8*(1), 161–184. Retrieved from `https://www.annualreviews.org/doi/10.1146/annurev-marine-010814-015912` doi: 10.1146/annurev-marine-010814-015912

Mahadevan, A., Pascual, A., Rudnick, D. L., Ruiz, S., Tintoré, J., & D'Asaro, E. (2020, jan). Coherent pathways for vertical transport from the surface ocean to interior. *Bulletin of the American Meteorological Society*, *101*(11), E1996–E2004. doi: 10.1175/BAMS-D-19-0305.1

Mahadevan, A., & Tandon, A. (2006). An analysis of mechanisms for submesoscale vertical motion at ocean fronts. *Ocean Modelling*, *14*(3-4), 241–256. doi: 10.1016/j.ocemod.2006.05.006

McWilliams, J. C. (2016, may). *Submesoscale currents in the ocean* (Vol. 472) (No. 2189). Royal Society of London. doi: 10.1098/rspa.2016.0117

McWilliams, J. C. (2021, jan). Oceanic Frontogenesis. *Annual Review of Marine Science*, *13*(1), 227–253. Retrieved from `https://www.annualreviews.org/doi/10.1146/annurev-marine-032320-120725` doi: 10.1146/annurev-marine-032320-120725

Omand, M. M., D'Asaro, E. A., Lee, C. M., Perry, M. J., Briggs, N., Cetinić, I., & Mahadevan, A. (2015). Eddy-driven subduction exports particulate organic carbon from the spring bloom. *Science*, *348*(6231), 222–225. doi: 10.1126/science.1260062

Pietri, A., Capet, X., D'ovidio, F., Levy, M., Sommer, J. L., Molines, J. M., & Giordani, H. (2021, mar). Skills and limitations of the adiabatic omega equation: How effective is it to retrieve oceanic vertical circulation at mesoscale and submesoscale? *Journal of Physical Oceanography*, *51*(3), 931–954. doi: 10.1175/JPO-D-20-0052.1

Ratner, B. (2009, jun). The correlation coefficient: Its values range between 1/1, or do they. *Journal of Targeting, Measurement and Analysis for Marketing*, *17*(2), 139–142. doi: 10.1057/jt.2009.5

Rocha, C. B., Gille, S. T., Chereskin, T. K., & Menemenlis, D. (2016, nov). Seasonality of submesoscale dynamics in the Kuroshio Extension. *Geophysical Research Letters*, *43*(21), 11,304–11,311. doi: 10.1002/2016GL071349

Saha, S., Moorthi, S., Pan, H.-L., Wu, X., Wang, J., Nadiga, S., . . . Goldberg, M. (2010). The NCEP Climate Forecast System Reanalysis. *Bulletin of the American Meteorological Society*, *91*(8), 1015–1058. Retrieved from `https://journals.ametsoc.org/view/journals/bams/91/8/2010bams3001_1.xml` doi: https://doi.org/10.1175/2010BAMS3001.1

Sanders, R., Henson, S. A., Koski, M., De La Rocha, C. L., Painter, S. C., Poulton, A. J., . . . Martin, A. P. (2014, dec). The Biological Carbon Pump in the North Atlantic. *Progress in Oceanography*, *129*(PB), 200–218. doi: 10.1016/j.pocean.2014.05.005

Shchepetkin, A. F., & McWilliams, J. C. (2005). The regional oceanic modeling system (ROMS): A split-explicit, free-surface, topography-following-coordinate oceanic model. *Ocean Modelling*, *9*(4). doi: 10.1016/j.ocemod.2004.08.002

Shcherbina, A. Y., D'Asaro, E. A., Lee, C. M., Klymak, J. M., Molemaker, M. J., & McWilliams, J. C. (2013, sep). Statistics of vertical vorticity, divergence, and strain in a developed submesoscale turbulence field. *Geophysical Research Letters*, *40*(17), 4706–4711. Retrieved from `http://doi.wiley.com/10.1002/grl.50919` doi: 10.1002/grl.50919

Siegelman, L., Klein, P., Rivière, P., Thompson, A. F., Torres, H. S., Flexas, M., & Menemenlis, D. (2020, jan). Enhanced upward heat transport at deep submesoscale ocean fronts. *Nature Geoscience*, *13*(1), 50–55. doi: 10.1038/s41561-019-0489-1

Siegelman, L. I. (2020, mar). Energetic submesoscale dynamics in the ocean interior. *Journal of Physical Oceanography*, *50*(3), 727–749. doi: 10.1175/JPO-D-19-0253.1

Stukel, M. R., Aluwihare, L. I., Barbeau, K. A., Chekalyuk, A. M., Goericke, R., Miller, A. J., … Landry, M. R. (2017, feb). Mesoscale ocean fronts enhance carbon export due to gravitational sinking and subduction. *Proceedings of the National Academy of Sciences of the United States of America*, *114*(6), 1252–1257. Retrieved from `https://pnas.org/doi/full/10.1073/pnas.1609435114` doi: 10.1073/pnas.1609435114

Takahashi, T., Sutherland, S. C., Sweeney, C., Poisson, A., Metzl, N., Tilbrook, B., … Nojiri, Y. (2002, jan). Global sea-air CO2 flux based on climatological surface ocean pCO2, and seasonal biological and temperature effects. *Deep-Sea Research Part II: Topical Studies in Oceanography*, *49*(9-10), 1601–1622. doi: 10.1016/S0967-0645(02)00003-6

Taylor, R. (1990, jan). Interpretation of the Correlation Coefficient: A Basic Review. *Journal of Diagnostic Medical Sonography*, *6*(1), 35–39. doi: 10.1177/875647939000600106

Treguier, A. M., Theetten, S., Chassignet, E. P., Penduff, T., Smith, R., Talley, L., … Böning, C. (2005, may). The North Atlantic subpolar gyre in four high-resolution models. *Journal of Physical Oceanography*, *35*(5), 757–774. doi: 10.1175/JPO2720.1

Uchida, T., Balwada, D., Abernathey, R., McKinley, G., Smith, S., & Lévy, M. (2019, dec). The Contribution of Submesoscale over Mesoscale Eddy Iron Transport in the Open Southern Ocean. *Journal of Advances in Modeling Earth Systems*, *11*(12), 3934–3958. Retrieved from `https://agupubs.onlinelibrary.wiley.com/doi/10.1029/2019MS001805` doi: 10.1029/2019MS001805

Vic, C., Hascoët, S., Gula, J., Huck, T., & Maes, C. (2022). Oceanic Mesoscale Cyclones Cluster Surface Lagrangian Material. *Geophysical Research Letters*, *49*(4), e2021GL097488. Retrieved from `https://agupubs.onlinelibrary.wiley.com/doi/abs/10.1029/2021GL097488` doi: https://doi.org/10.1029/2021GL097488

Wang, L., Gula, J., Collin, J., & Mémery, L. (2022, jul). Effects of Mesoscale Dynamics on the Path of Fast-Sinking Particles to the Deep Ocean: A Modeling Study. *Journal of Geophysical Research: Oceans*, *127*(7), e2022JC018799. Retrieved from `https://onlinelibrary.wiley.com/doi/10.1029/2022JC018799` doi: 10.1029/2022JC018799

Wenegrat, J. O., Thomas, L. N., Sundermeyer, M. A., Taylor, J. R., D'Asaro, E. A., Klymak, J. M., … Lee, C. M. (2020, jul). Enhanced mixing across the gyre boundary at the Gulf Stream front. *Proceedings of the National Academy of Sciences of the United States of America*, *117*(30), 17607–17614. doi: 10.1073/pnas.2005558117

Seasonal tracer subduction in the Subpolar North Atlantic driven by submesoscale fronts

Théo Picard[1], Jonathan Gula[2,3], Clément Vic[2], Laurent Mémery [1]

[1]Univ Brest, CNRS, IRD, Ifremer, Laboratoire des Sciences de l'Environnement Marin (LEMAR), IUEM, Plouzané, France
[2]Univ Brest, CNRS, IRD, Ifremer, Laboratoire d'Océanographie Physique et Spatiale (LOPS), IUEM, Plouzané, France
[3]Institut Universitaire de France (IUF), Paris, France

Key Points:

- Surface strain and vorticity criteria can be used to identify submesoscale fronts.
- The tracer depth injection correlates with density of fronts, regardless of the mixed layer depth evolution.
- The submesoscale fronts contribute to $\sim 40\%$ of the vertical advective subduction in winter, and less than 1% in summer.

Corresponding author: Théo Picard, theo.picard@univ-brest.fr

Abstract

Submesoscale flows (0.1 - 10 km) are often associated with large vertical velocities, which can have a significant impact on the transport of surface tracers, such as carbon. However, global models do not adequately account for these small-scale effects, which still require a proper parameterization. In this study, we introduced a passive tracer into the mixed layer of the northern Atlantic Ocean using a CROCO simulation with a high horizontal resolution of $\Delta x = 800$ m, aiming to investigate the seasonal submesoscale effects on vertical transport. Using surface vorticity and strain criteria, we identified regions with submesoscale fronts and quantified the associated subduction, that is the export of tracer below the mixed layer depth. The results suggest that the tracer vertical distribution and the contribution of frontal subduction can be estimated from surface strain and vorticity. Notably, we observed significant seasonal variations. In winter, the submesoscale fronts contribute up to 40% of the vertical advective transport of tracer below the mixed layer, while representing only 5% of the domain. Conversely, in summer, fronts account for less than 1% of the domain and do not contribute significantly to the transport below the mixed layer. The findings of this study contribute to a better understanding of the seasonal water subduction due to fronts in the region.

Plain Language Summary

Small ocean movements known as submesoscale fronts are often overlooked in global models. These flows, ranging from 0.1 to 10 kilometers, play a big role in how carbon, nutrient or heat are transported inside the ocean. To better understand the influence of submesoscale fronts, we use a fine scale numerical simulations in the North Atlantic. We added a tracer in the ocean upper-layer to analyse how it gets transported at depth. Using criteria of surface rotation speed and how water gets stretched, we identify the areas of submesoscale fronts. We observed that the depth at which the tracer is injected depend on the density of submesoscale fronts. Also, the study results show that these flows exhibit interesting seasonal variations. In winter, the submesoscale fronts contribute up to 40% to the vertical transport of carbon, even though they only cover 5% of the studied area. Conversely, in summer, fronts represent less than 1% of the area and don't significantly impact the vertical tracer transport. This study helps us better understand how water moves in the ocean, especially across different seasons. This understanding could be key to addressing questions related to climate change and how substances like carbon are distributed in the world's oceans.

1 Introduction

There is an on-growing set of evidence that submesoscale physical processes actually matter for the transport of oceanic tracers such as heat, carbon and nutrients (Klein & Lapeyre, 2009; Omand et al., 2015; Stukel et al., 2017; Llort et al., 2018; Lévy et al., 2018; Boyd et al., 2019; Lacour et al., 2019). Submesoscale phenomena are characterised by frontal and filamentary structures with lateral scales ranging from 1 to 10 km. These structures typically arise from mesoscale eddy stirring and baroclinic instability at the ocean surface, exhibiting Rossby ($Ro = \zeta/f$) numbers on the order of 1 (Lévy et al., 2024). The frontogenesis, responsible for ageostrophic flow known as secondary circulation, induces strong and deep vertical velocities localised precisely at the front (McWilliams, 2021; Gula, Taylor, et al., 2021). Fronts are characterised by a dense cyclonic side with downward velocities and a light anticyclonic side with upward velocities. In the context of the carbon cycle, this results in a double contribution : On the one hand, it drives nutrients, essential for the primary production, from the (interior) twilight zone into the euphotic layer (Lapeyre Guillaume, 2006; Lévy et al., 2018; Mahadevan, 2016). On the other hand, it facilitates the subduction of surface carbon (transport below the mixed layer) along isopycnal pathways, effectively storing it for extended periods (Wenegrat et al., 2020; Mahadevan et al., 2020; Freilich & Mahadevan, 2021). Concerning heat transport, L. Siegelman et al. (2020) demonstrated that fronts actively participate in the upward heat transport from the ocean interior to the surface and are essential ingredients of the Earth's heat budget.

While it is clear that fronts play a significant role in tracer budgets, the vertical transport induced by submesoscale processes remains unresolved and is not yet parameterized in climate models (Bopp et al., 2013; Mahadevan et al., 2020). Overcoming this challenge is one of the major hurdles in ocean modeling (Fox-Kemper et al., 2019). However, although there has been recent interest in quantifying the submesoscale contribution to tracer transport, there is still no clear consensus on its impact. A major obstacle is the difficulty of sampling submesoscale processes using remote sensing and in situ observational instruments. Indeed, satellite altimetry can only detect structures larger than 100 kilometers (Chelton et al., 2011), and the measurement of vertical transport due to small-scale phenomena in the ocean remains a challenge (Mahadevan et al., 2020). The computation of submesoscale velocity gradient generally requires multiple ships, autonomous underwater vehicles, or surface drifters (Shcherbina et al., 2013; Gula, Taylor, et al., 2021). With respect to numerical simulations, it has been shown that fine-scale ocean regional circulation models with subkilometer horizontal grid spacing can accurately capture submesoscale dynamics (Mahadevan & Tandon, 2006; Capet et al., 2008; Pietri et al., 2021). However, high-resolution modeling is constrained by computational costs (Lévy et al., 2024), resulting in spatial limitations and/or idealized setups.

Various methodologies have been proposed to assess the frontal contribution, particularly in the context of carbon export. Balwada et al. (2018) estimated that the subduction could be doubled by comparing models with 20 and 1 km horizontal resolution. Uchida et al. (2019) quantified the ageostrophic contribution using spectral analysis and found that submesoscale structures could account for about a third of the total fluxes. In Freilich and Mahadevan (2021), Lagrangian particles were used to identify particles trapped in submesoscale structures. Their findings showed that 7.7% of the particles are subducted from the mixed layer, with subduction occurring mainly in localized regions along fronts. Based on glider observations during the North Atlantic bloom and supported by numerical modeling, Omand et al. (2015) showed that submesoscale structures can contribute up to half of the total spring export of particulate organic carbon (POC). In a recent study, Balwada et al. (2021) used Joint Probability Density Function (JPDF) of surface vorticity and strain on an idealized fine-scale model of the Antarctic Circumpolar Current to identify fronts. Their research showed that submesoscale fronts, although occupying only about 5% of the surface domain, could potentially account for up to 20% of the vertical transport at the Mixed Layer Depth (MLD). This wide range of results underlines the complexity and considerable uncertainties associated with this topic.

Despite this growing body of literature, there is a notable gap in knowledge as most studies tend to overlook the seasonal variability of these phenomena. However, it is now clear that submesoscales exhibit a strong seasonal cycle (Callies et al., 2015; Rocha et al., 2016; Berta et al., 2020). Futhermore, the modulation of tracer export on seasonal time scales has recently been demonstrated (Cao & Jing, 2022; Mahadevan et al., 2020). Therefore, the primary objective of our study is to assess the seasonal impact of submesoscale processes on a passive tracer released in the mixed layer (ML) using a highly realistic model. In particular, we focus on the North Atlantic subpolar gyre, a region known for significant seasonal variations. Moreover, this region is particularly important as being one of the most critical areas for carbon sequestration, with an average uptake of about $0.55{-}1.94 PgCyear^{-1}$, which represents $\sim 12\%$ of the global net ocean uptake (Takahashi et al., 2002; Sanders et al., 2014), and with significant phytoplankton blooms in spring, when submesoscale activity is intense (Treguier et al., 2005; Le Corre et al., 2020).

The outline of this paper is as follows. Section 2 presents our numerical simulation. Section 3 outlines the methodology used to identify seasonal surface submesoscale fronts.

Section 4 describes the seasonal evolution of a tracer released within the ML and analyzes the contribution of fronts to tracer subduction. Finally, section 5 provides a detailed discussion of the results.

2 Methodology

2.1 Numerical setup

We set up a realistic simulation of the circulation in a northeastern part of the North Atlantic subpolar gyre, using the oceanic modeling system CROCO (Coastal and Regional Ocean COmmunity model), which resolves the primitive equations (Shchepetkin & McWilliams, 2005). A nesting approach is used here with a parent simulation (GIGATL3) covering most of the Atlantic Ocean with a horizontal resolution of 3 km (Gula, Theetten, et al., 2021). GIGALT3 provides the nested simulation with the initial state and the lateral boundary conditions. The study domain is shown in Figure 1. It covers an area of 800 km $\times$ 640 km, ranging from 53.8 N to 62.5°N and from 20.5°W to 37.8°W. The horizontal grid spacing $\Delta x = 800$ m is almost constant across the domain. Vertically, we discretize the model with 200 sigma levels, which roughly corresponds to cell heights of $\Delta z = 2$ m within the surface layer. This vertical resolution is chosen to accurately represent the surface dynamics. The ocean is forced at the surface by hourly atmospheric forcings from the Climate Forecast System Reanalysis using a bulk formulation with relative winds (Saha et al., 2010). Tidal forcing is not included. The grid bathymetry is from the global SRTM30plus dataset (J. J. Becker D. T. Sandwell & Weatherall, 2009). The simulation is run for 13 months, from December 1, 2007, to December 31, 2008, with a time step of 90 seconds and produces 3-hourly averaged outputs. The first month is dedicated to the spin-up phase, ensuring that submesoscale structures have time to develop. We therefore analyse the outputs for the year 2008. To discard boundary effects, all the results are computed within a subdomain excluding points within 100 km of the boundaries.

2.2 Tracer initialisation and equation

On the first day of each month, a passive tracer is released throughout the entire domain within the upper mixed layer (ML) and remains for a period of 29 days. This experimental design allows us to evaluate and compare both ML water subduction and deep export independently for each month. The MLD is determined by computing a density threshold of 0.03 kg m^{-3} from the surface, as described in de Boyer Montégut et al. (2004). We distribute the tracer concentration C following a hyperbolic tangent profile:

$$C(x, y, z, t = 0) = \frac{1}{2}\left(1 + \tanh\left(\frac{z - z_{target}}{dz(x, y)}\right)\right). \qquad (1)$$

Where x, y, z are the spatial coordinates, and t is the time. We choose $z_{target} = 0.6 \cdot z_{mld}(x, y)$ to ensure that there is no tracer below the MLD. In addition, $dz = \frac{-z_{mld}(x,y)}{8}$ is chosen to achieve a smooth transition near the MLD to avoid numerical instability due to sharp vertical gradients in tracer concentration. Figure 2 shows an example of the tracer concentration for 3 selected days in February. It illustrates how the tracer is stirred by the mesoscale and submesoscale circulation and how it accumulates or is depleted from frontal regions.

The CROCO model uses the following tracer equation:

$$\frac{\partial C}{\partial t} = -u_j \frac{\partial C}{\partial x_j} - w \frac{\partial C}{\partial z} + \nu_c + D_c + S_c, \qquad (2)$$

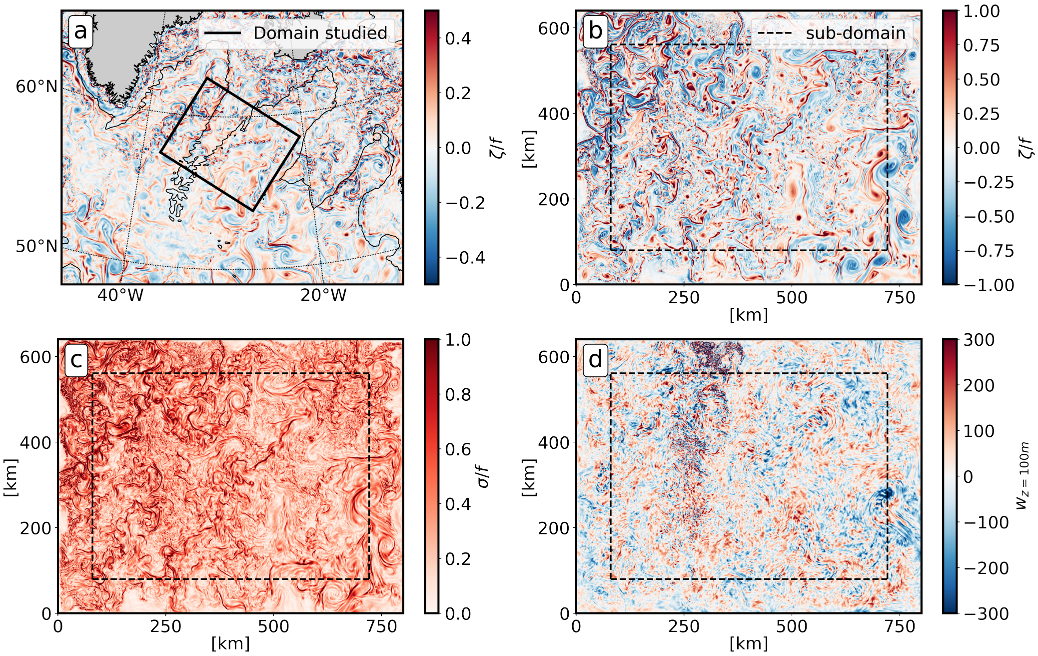

Figure 1. (a) Snapshot of the GIGATL3 simulation (dx = 3km) on the 8th of February . The background is the relative vorticity and the black contour is the bathymetry at 2000 m. The black rectangle is the domain of the regional simulation. (b), (c) and (d) represent the relative vorticity, the strain and vertical velocities at 100 m depth, respectively, computed from the regional simulation (dx = 800m). The relative vorticity and strain are normalised to the local Coriolis frequency. All the statistical results are computed in the dashed rectangle subdomain to discard boundary effects.

where C is the tracer concentration, u_j are the horizontal velocities, w is the vertical velocity, ν_c is the vertical diffusion, D_c is the horizontal diffusion and S_c is a source or sink term (set to zero in this study). D_c is not explicit in CROCO, but results from the implicit contribution of the upstream-biased advection scheme. Vertical mixing ($\nu_c = \frac{\partial}{\partial z}(K_c \frac{\partial C}{\partial z})$ computed with the tracer diffusivity K_c is parameterized with the KPP scheme (Large et al., 1994).

3 Seasonality of submesoscale fronts

The numerical simulation provides compelling evidence for tracer subduction driven by fronts. Figure 3 presents a vertical section of the domain on April 3rd, 3 days after the tracer release. The vertical section highlights a distinct front characterized by a significant increase in vertical velocity (w > 100 m/d) and a pronounced subduction of the tracer below the mixed layer. In this section, we first explain how we identify submesoscale fronts based on a strain and vorticity criterion and we present a first analysis to quantify the seasonal variations in the prevalence of fronts and their associated velocity field.

3.1 Seasonal variability of submesoscale fronts

The dynamics of the horizontal flow can be expressed in terms of the strain tensor. This strain tensor can be decomposed into the vertical vorticity ζ, the horizontal

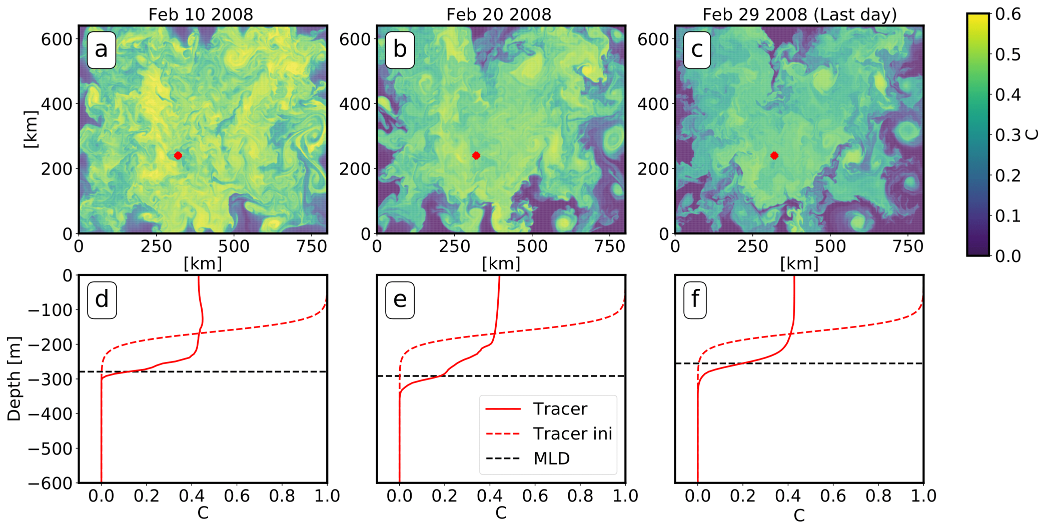

Figure 2. (a), (b) and (c) show the tracer concentration at the surface for February 10, 20 and 29. (d), (e) and (f) show the corresponding tracer vertical distribution (red line) at the location of the red dot. The dashed red line shows the initial vertical distribution of the tracer and the dashed black line is the MLD.

divergence δ and the strain rate σ (referred to as strain in the following for simplicity) as follows:

$$\zeta = \frac{\partial v}{\partial x} - \frac{\partial u}{\partial y} \quad ; \quad \delta = \frac{\partial u}{\partial x} + \frac{\partial v}{\partial y} \quad ; \quad \sigma = \sqrt{\left(\frac{\partial u}{\partial x} - \frac{\partial v}{\partial y}\right)^2 + \left(\frac{\partial u}{\partial y} + \frac{\partial v}{\partial x}\right)^2} \quad . \tag{3}$$

Strain and vorticity are often used to identify structures such as submesoscale fronts and eddies. Figure 1 displays the vorticity and strain within the domain on 8th February. During this winter period, we observe widespread and intense submesoscale structures, which are characterized by high vorticity and strain. This signature distinguishes them from eddy structures, which typically exhibit significant vorticity but weak strain patterns (Gula et al., 2014). Therefore, a flow decomposition based on joint probability density functions of surface vorticity and strain proves valuable for identifying fronts and eddies (Shcherbina et al., 2013). Previous studies have localized submesoscale fronts in vorticity-strain space as the regions near the lines $\sigma = |\zeta|$ (Shcherbina et al., 2013; McWilliams, 2016; Balwada et al., 2021). In a strongly ageostrophic regime ($|\delta| \sim |\zeta|$; Gula et al. (2014)), Barkan et al. (2019) demonstrated that fronts tend to cluster around the lines $\sigma = \sqrt{2}|\zeta|$. However, to our knowledge, none of the previous studies have precisely defined the area corresponding to submesoscale fronts. We have therefore chosen to define the frontal region by $\sigma > |\zeta|$ and with a restrictive criterion of $|\zeta/f| \sim Ro > 0.5$. The Ro criterion is based on the work of L. I. Siegelman (2020), who observed in a fine resolution model that submesoscale structures above the permanent thermocline characterised by ageostrophic flow are associated with $Ro > 0.5$. We define two subdomains, labelled 1A and 1C and delineated by dots and hatches, respectively, corresponding to the anticyclonic and cyclonic submesoscale fronts (Figure 4). The separation of cyclonic and anticyclonic fronts is useful because cyclonic fronts (1C) are known to contribute significantly to intense downward velocities, while anticyclonic fronts generally induce upwelling and weaker velocities (Gula, Taylor, et al., 2021). In addition, we name the two other zones dominated by vorticity based on Balwada et al. (2021): the anticy-

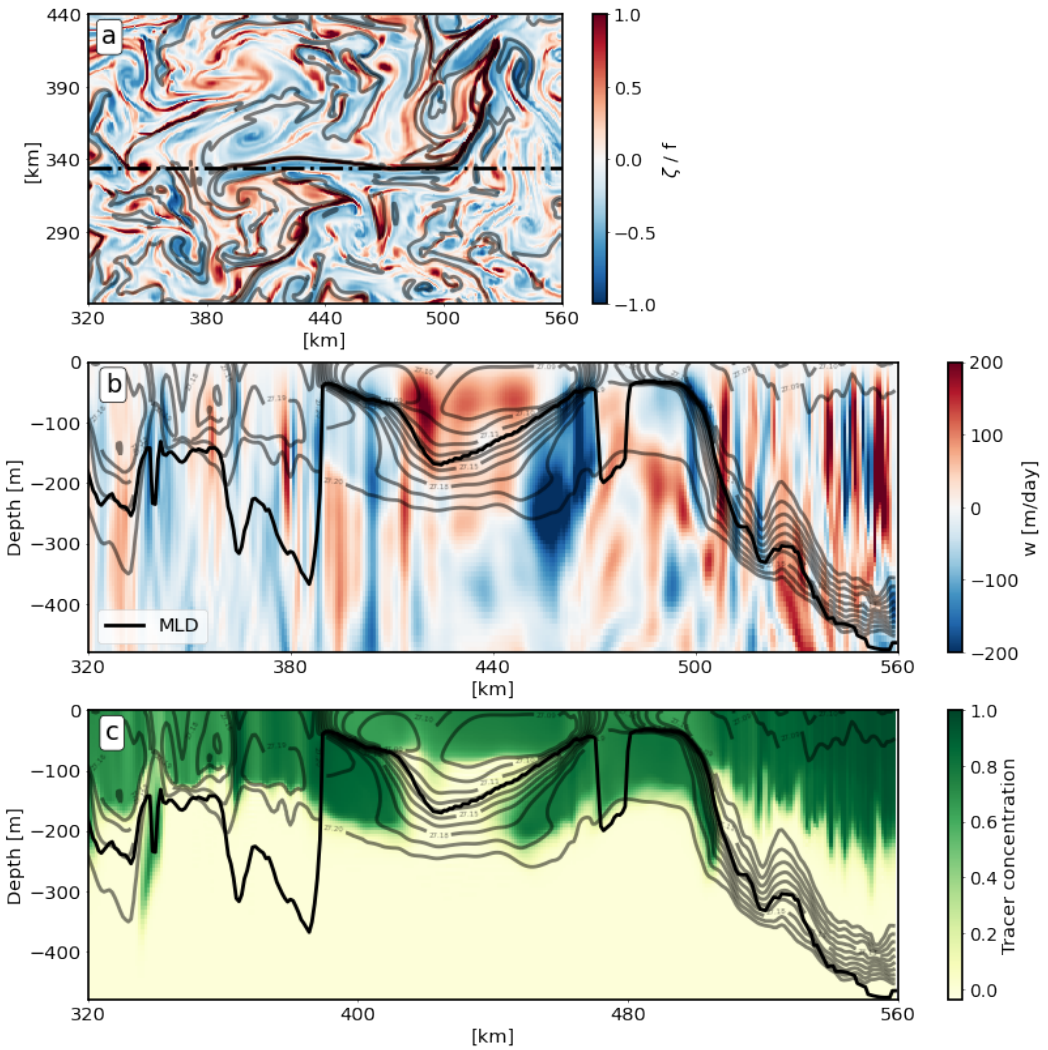

Figure 3. (a) Snapshot of the surface relative vorticity on the 3rd of April. The vertical section over a front is marked with a dashed black line. (b) Vertical cross section. The colors represent the vertical velocities. The black line is the MLD computed with a density threshold. The grey lines are the isopycnals. c) Tracer concentration on the same vertical section.

clonic zone (2) defined by $\zeta/f > 0$ and $\sigma < |\zeta|$, and the cyclonic zone, defined by $\zeta/f < 0$ and $\sigma < |\zeta|$. These regions correspond to areas within anticyclonic and cyclonic eddies.

Figure 4a displays the integrated surface strain-vorticity JPDF computed over March 2008. These statistics are computed within bins of size of 0.05×0.025 (vorticity $\times$ strain). The contour line delineates the region containing 99,99% of the grid points. A large fraction of the surface points exhibit weak vorticity and strain ($\zeta/f < 0.5$ and $\sigma/f < 0.5$), consistent with the quasi-geostrophic regime of turbulence expected to develop at this model resolution. The observed asymmetry, characterised by a peak in 1C, is the signature of submesoscale fronts (McWilliams, 2016; Buckingham et al., 2016). The 99.99% contour of the surface vorticity-strain JPDF is shown for each month in Figure 4b). Each season has a distinct JPDF signature, reflecting a clear shape evolution driven by the presence of submesoscale dynamics. The winter period exhibits the largest domain with

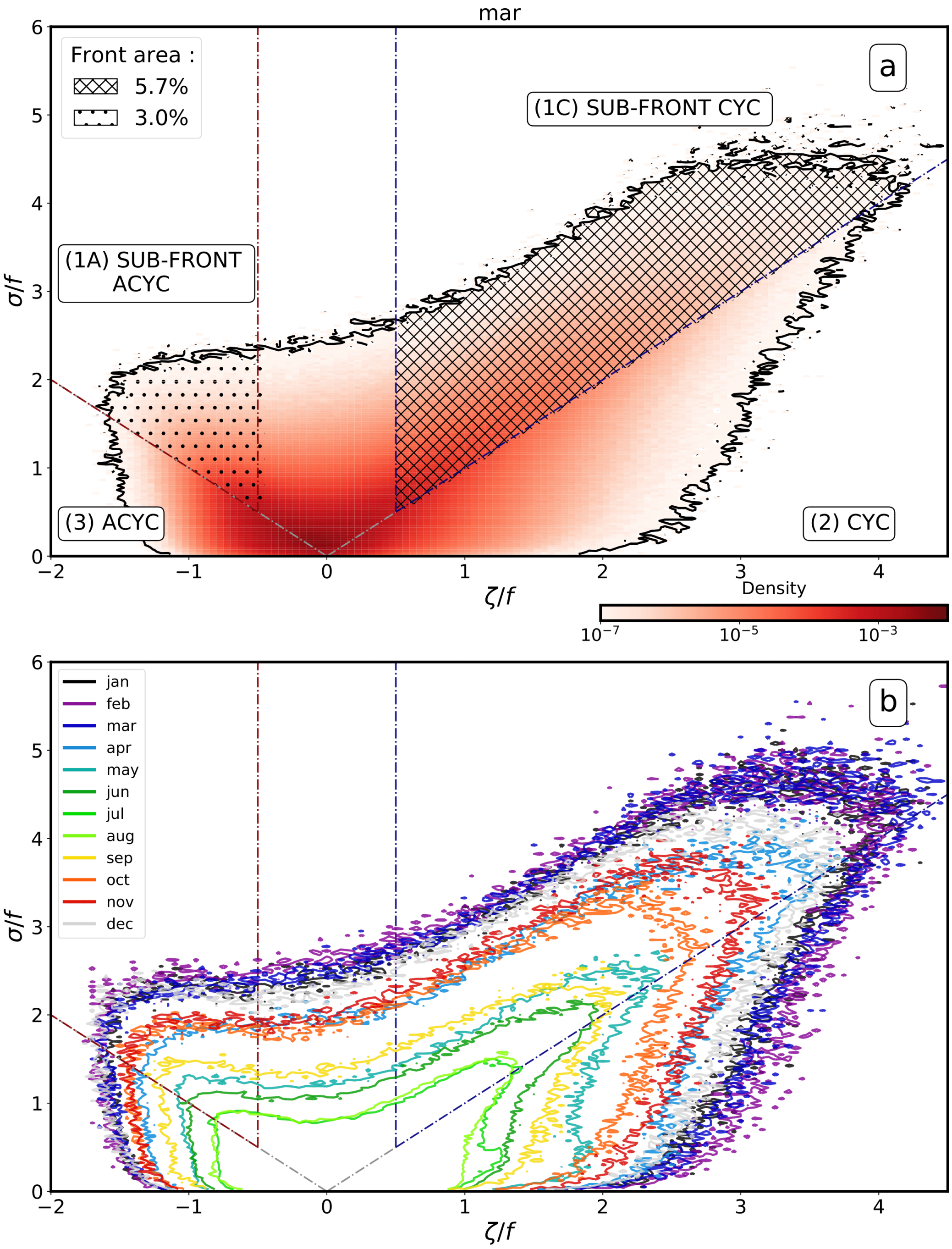

Figure 4. (a) Surface strain - vorticity JPDF in March. The black contour is the integrated domain containing 99.99% of the points. (1A) is the anticyclonic submesoscale frontal zone and (1C) is the cyclonic submesoscale frontal zone. (2) and (3) are the cyclonic and anticyclonic zones, respectively. The proportion of points within 1A (dotted area) and 1C (hatched area) are given. (b) Surface strain - vorticity JPDF domain contours (99.99% of the points) for each month.

the highest asymmetry due to more energetic submesoscales (Callies et al., 2015), while the JPDF envelope during the summer months is confined to a region of low strain and

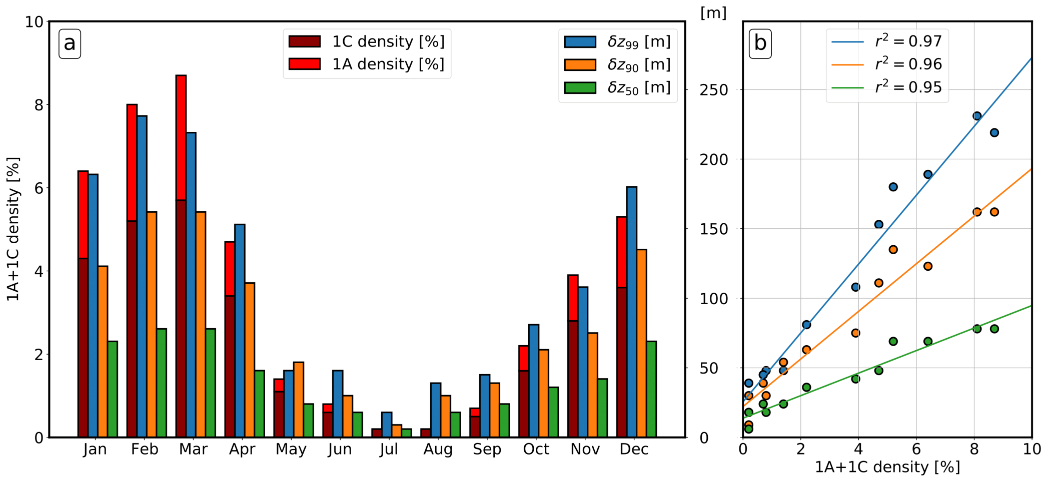

Figure 5. a) Deepening of the 50th (green), 90th (orange) and 99th (blue) tracer percentiles between the first and last day for each monthly experience. Red bars are the fraction of points within 1A and 1C. b) Linear regression between front density and tracer depth.

vorticity. Interestingly, the peak remains significant in spring, making this period particularly relevant for organic carbon export as the region hosts significant phytoplankton blooms in the euphotic layer. To quantitatively assess the presence of fronts, we calculate the fraction of points within regions 1A + 1C for each month, which we consider to be the front density (Figure 5a). The frontal area is maximum in March, accounting for about 9% of the total area (5.7 % in 1C). Conversely, the lowest fraction of submesoscales is found in July with less than 0.5%.

3.2 Seasonal variability of vertical velocity

Following the approach in Balwada et al. (2021), we look at the distribution of variables at depth as a function of surface vorticity and strain. This approach reveals interesting patterns in the vertical velocity w. For each month, we computed the distribution of the bin-averaged vertical velocity $\langle w_z \rangle$, conditioned on surface vorticity and strain over 20 vertical z levels equally spaced from the surface to 2×MLD. An example for March is shown in Figure 6. Similar to the density JPDF, we use 3-hourly outputs (averages) during the first 29 days of each month. Our approach is similar to that of Balwada et al. (2021), with a key difference being that instead of considering a horizontally constant MLD, we compute the MLD at each grid point and for each time step.

The cyclonic part is generally associated with $\langle w \rangle < 0$. The largest negative velocities are within the 1C area and persist down to depths of $2\times MLD$. For the anticyclonic area, $\langle w \rangle$ is generally positive near the surface, regardless of fronts or eddies. However, some observations change below the MLD. First, the velocities inside the eddy area ($|\zeta| > |\sigma|$) become much weaker, while the velocities inside the frontal area remain significant. We also observe a shift in the sign of the velocities in 1A close to the MLD and below. This shift is a direct consequence of the methodological limitation. Indeed, the dynamics conditioned at depth, especially below the MLD, may not always be directly linked to surface properties. First, the fronts are often surface intensified and the associated second circulation may not extend to the MLD and below. In addition, vertical velocities induced by a front often follow isopycnal paths that are not vertical and include a horizontal component (Freilich & Mahadevan, 2021). Consequently, the associated subduction may not necessarily be located directly beneath its apparent surface signature, and lateral advection transport may also be induced. This is particularly problematic for the light anticyclonic side of fronts, whose upward path may be above the dense cyclonic downward path (Figure A1). Consequently, below a certain depth, we associate part of the cyclonic downward velocity with the 1A area, biasing the results, especially for months associated with deep MLDs such as March.

Focusing on the frontal areas, we compare the vertical profiles of vertical velocity for each month. We compute the density-weighted mean $\langle w \rangle$ (i.e. the mean velocities weighted by the corresponding bin density) for 1C and 1A over the vertical (Figure 7a,b). The maximum velocities within the fronts are typically observed at depths corresponding to 0.3-0.4 $\times$ MLD, and usually drop to a much weaker value near the MLD. Region 1C is consistently associated with downwelling, with varying seasonal intensities ranging from -130 m/day (winter) to -10 m/day (summer). In contrast, region 1A shows upwelling with values ranging from 5 m/day to 70 m/day. Below the MLD, $\langle w \rangle$ remains consistently negative in 1C, while in 1A, $\langle w \rangle$ can change sign below 1.1 $\times$ MLD. We observe such a transition from positive to negative values below $1.1 \times MLD$ from October to March, which are months associated with deep MLDs, presumably due to the bias mentioned above.

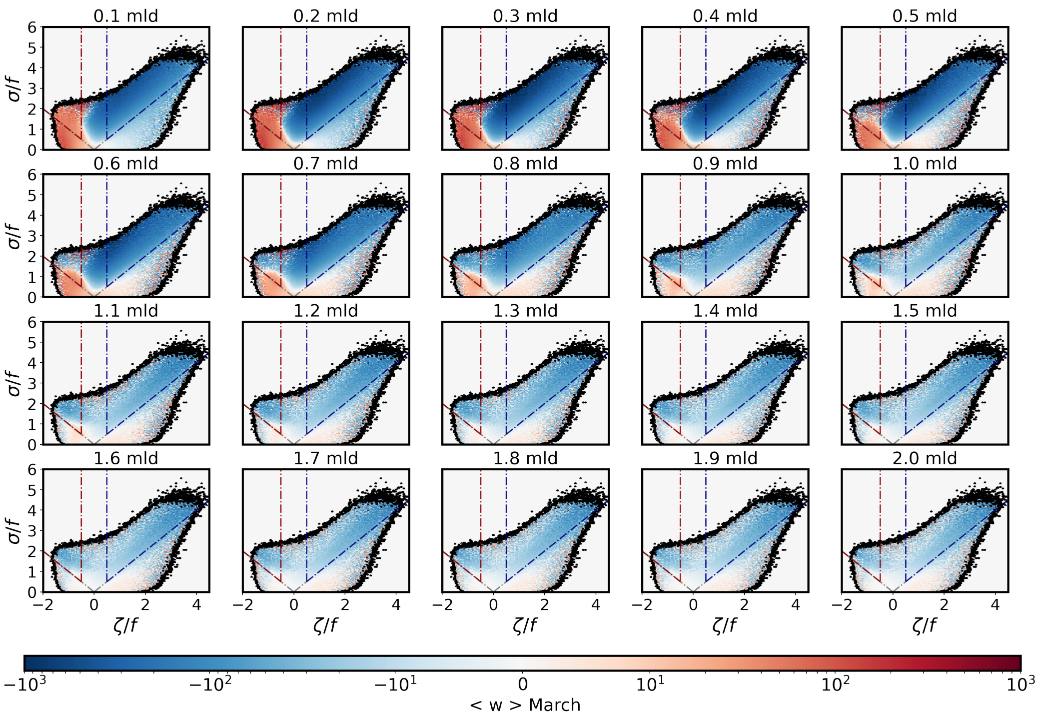

Figure 6. Bin-averaged vertical velocity conditionned on surface vorticity and strain at different vertical levels during March. The black contour is the integrated domain containing 99.99% of the points. The remaining 0.01% of points are hidden.

To analyse subduction, we focus in particular on the mean vertical velocity at the MLD $\langle w_{mld} \rangle$ Figure 8. Although there is a monthly variability in the distribution of $\langle w_{mld} \rangle$, we still observe a consistent pattern in the vertical velocity. Notably, both anticyclonic (3) and cyclonic (2) features are associated with positive vertical velocities. Cyclonic fronts in region 1C exhibit strong downward velocities, while anticyclonic fronts in region 1A exhibit a mixture of positive and negative vertical velocities. Most of the area of region 1A in strain-vorticity space has negative vertical velocities, but the area mean is still positive (Figure 7b) due to the much higher density of points in the lower strain and vorticity region associated with positive vertical velocities. However, with the exception of the 1A area, we observe robust w patterns constrained by surface dynamical features, independent of season and depth. These observations support our hypothesis that the surface dynamics are strongly linked to the vertical velocity at the MLD.

The mean vertical velocity also appears to follow a seasonal pattern. The relationship between the frontal area density and $\langle w_{mld} \rangle$ in 1A and 1C is shown in Figure 7c,d. It shows a moderate correlation with $r^2 = 0.37$ in 1C and $r^2 = 0.54$ in 1A (Taylor, 1990; Ratner, 2009), which suggests that vertical velocities are more intense at the MLD when front density is higher.

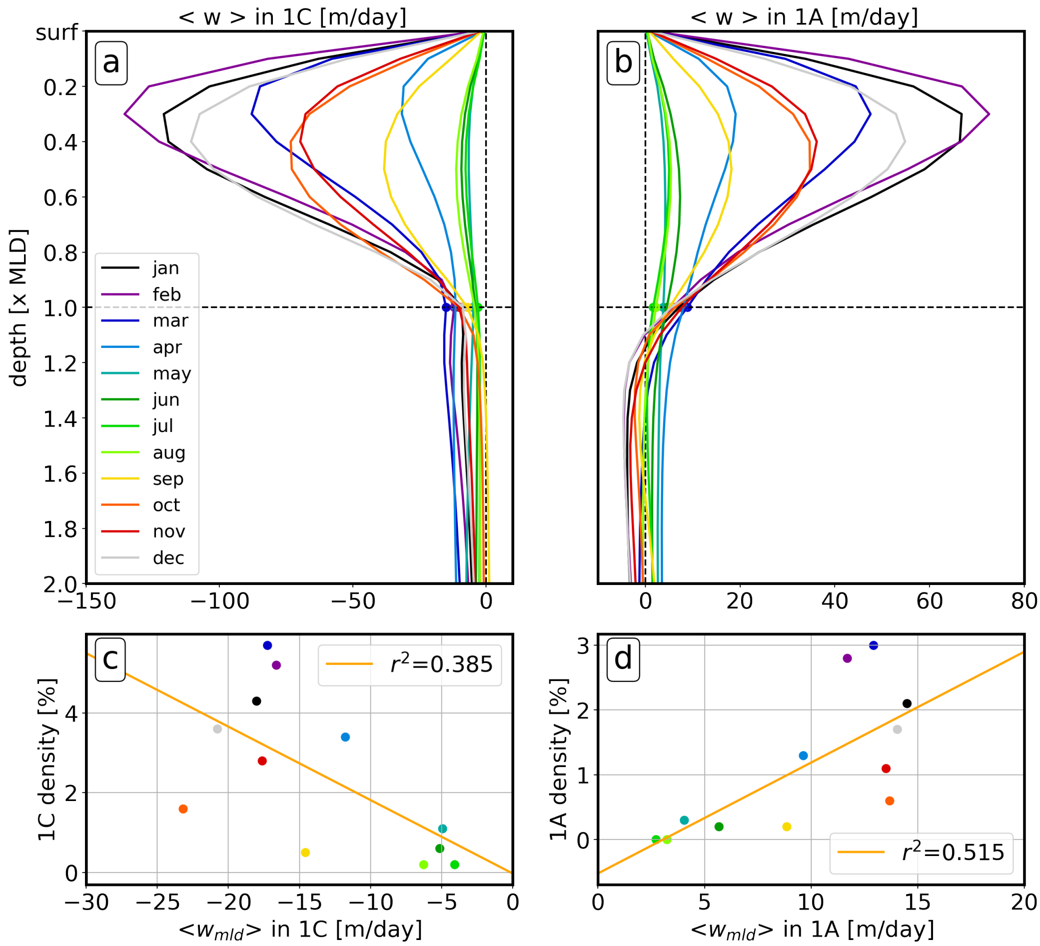

Figure 7. Mean vertical velocity $\langle w \rangle$ in 1A (a) and 1C (b) between the surface and 2 * MLD for each month. Linear regression between the mean velocity at MLD $\langle w_{mld} \rangle$ and the front density in 1A and 1C.

4 The seasonal tracer evolution

In this section we analyse the tracer transport at depth, focusing in particular on the vertical advective subduction that occurs within fronts.

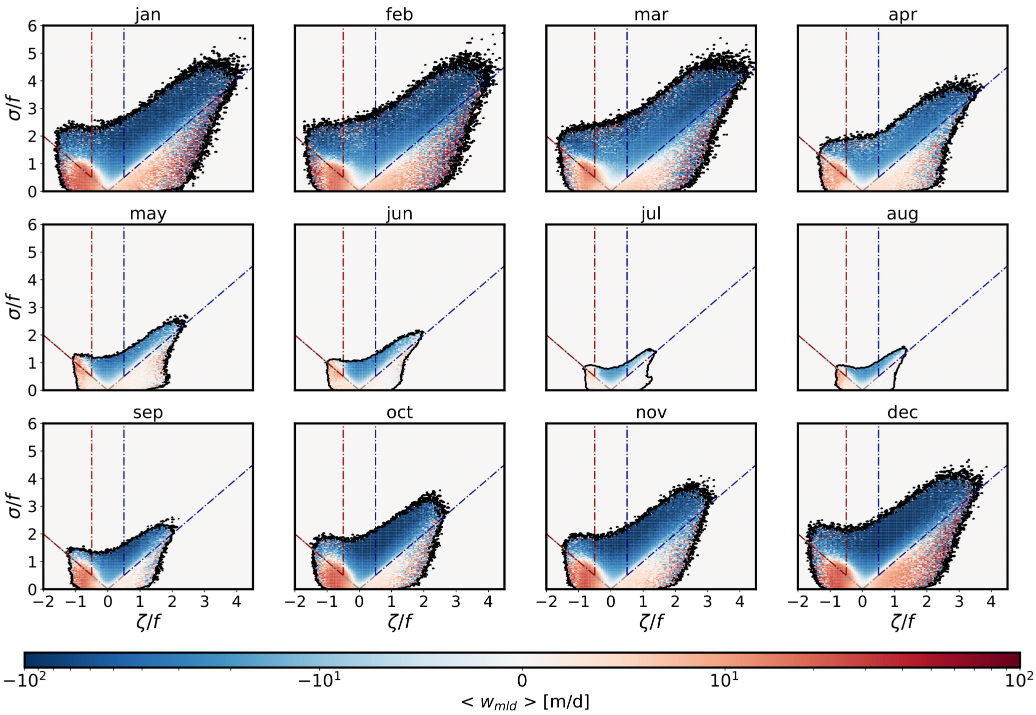

Figure 8. Surface strain-vorticity JPDF conditioned with the mean vertical velocity w at MLD and for each month. Black contour is the integrated domain that contain 99.99% of points (points outside have been removed).

4.1 Tracer deepening

We examine the tracer evolution over the vertical in Figure 9, which displays the average tracer concentration within 3-meter bins and the spatially averaged evolution of the mixed layer depth $\langle MLD \rangle$. Over the study period, the ML has a typical seasonal evolution characterised by a stable and large depth in winter, intense stratification in spring, a shallow and stable depth in summer and a gradual deepening in fall. To better estimate the evolution of the tracer, we compute the distribution of the tracer concentration as a function of depth and monitor the distribution's median, 90th, and 99th percentiles. Each month the tracer spreads deeper into the water column, and the concentration within the ML decreases. It is important to note that since the simulation has open boundaries, the tracer can escape through the boundaries, but this does not affect the statistical results. The tracer depth is particularly important for carbon export, as the carbon sequestration time is directly dependent on the depth of injection (Bol et al., 2018). The difference between the depth of each percentile on the first day and on the last day ($\delta z_{99}, \delta z_{90}, \delta z_{50}$) is plotted in Figure 5a. The varying seasonal conditions allowed us to compute the linear regression between the front density and the tracer deepening. Interestingly, δz_{99},δz_{90} and δz_{50} appear to be significantly correlated with the front density (Figure 5b). This suggests that the front density may impact the depth at which the tracer is subducted. Consequently, the surface conditions can potentially be used as an indicator to estimate the redistribution of tracer at depth in this region.

4.2 Seasonal tracer subduction driven by submesoscale fronts

To estimate the contribution of submesoscale fronts to tracer vertical transport, we mapped the vertical transport of the tracer, (wC), in surface strain-vorticity space

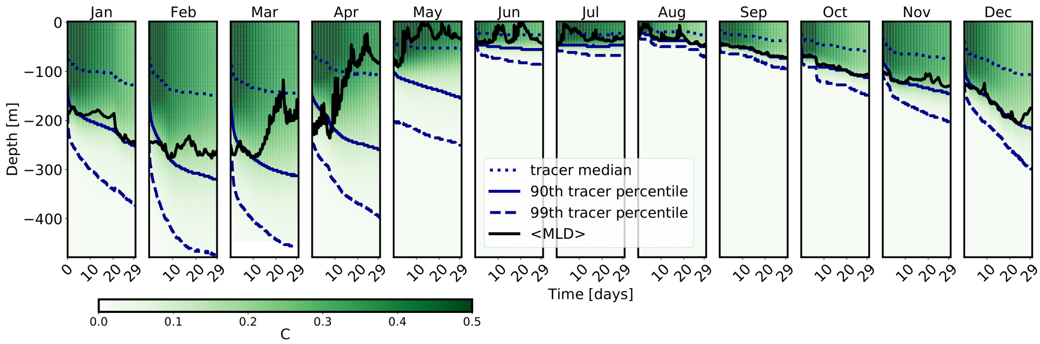

Figure 9. Tracer distribution and evolution for each month. The tracer concentration is vertically averaged over 3-meter bins. The black line is the spatial mean of the mixed layer depth computed for each time step (3h) with a density threshold. Blue lines represent the 50th (dotted), 90th (solid) and 99th (dashed) percentiles of the tracer.

– w represents the vertical velocity, and C is the tracer concentration. We computed the sum ΣwC within each bin and, similar to part 3.3, these results are computed for 20 vertical levels between the surface and z = 2 × MLD. An example for March is given in Figure 10. Inside the mixed layer, the vertical transport is similar to what we observe with velocity (Figure 6). This is because the tracer is almost uniform across the mixed layer and always positive. Therefore, the total transport is directly related to the mean velocity. Below the MLD, however, the transport is mostly negative in each region. This is because no tracer was injected at this depth during the initial conditions. A small part in the eddy region still shows positive transport, suggesting that some of the subducted tracer may be reinjected into the mixed layer. The blue contours indicate the region contributing to 50% and 99% of the downward transport. It is clear that most of the downward contribution is associated with low strain and vorticity, where the density is maximum 4. However, the 1C area also appears to be a region that contributes significantly to the export.

To confirm this trend, for each month and within the depth range between the surface and 2 × MLD, we calculated the total tracer fluxes inside 1A and 1C, i.e., the sum of the bins in 1A and 1C (Figures 11a and b). We also estimated the fraction of these fluxes relative to the total downward fluxes, i.e., $\frac{\Sigma wC_{1C}}{\Sigma wC_{wC<0}}$ and $\frac{\Sigma wC_{1A}}{\Sigma wC_{wC<0}}$ (Figures 11c and d). Similar to w, the transport wC in 1C and 1A reaches a peak at z = 0.3-0.4 MLD and decreases significantly near the MLD. In 1C, the transport remains always negative and can contribute significantly to the total downward transport between the surface and $2 \times MLD$. In 1A, however, the transport shifts from positive to negative precisely at the MLD. It is difficult to interpret the results in 1A below the MLD. As no tracer was injected below the MLD, no significant positive contribution can be observed. In addition, the negative export in this region may also also due to the bias mentioned in section 3.2.

Focusing on subduction, we plotted $w_{mld}C_{mld}$ conditioned on vorticity and strain for each month in Figure 12. Irrespective of the season, the anticyclonic (3) and cyclonic (2) areas contribute mainly to the upward transport, while the remaining region is associated with mainly downward transport. Again, we observe the important contribution of the 1C area, which participates mainly in the downward fluxes. The positive transport near the anticyclonic eddy boundary and the negative transport for intense strain in 1A seem to compensate each other as suggested by Figure 11 b).

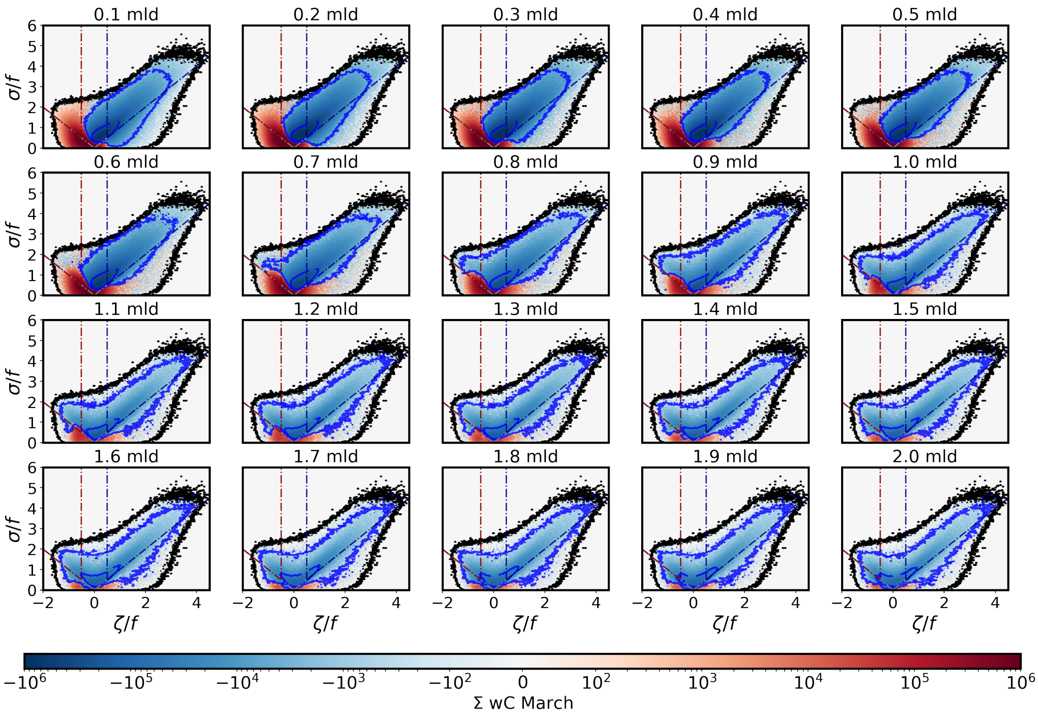

Figure 10. Surface strain-vorticity JPDF conditioned with the sum of vertical transport ΣwC at different vertical levels for March. Black contour is the integrated domain containing 99.99% of the points. Points outside have been removed. Blue contours include the integrated points contributing to 50% (inside) and 99% (outside) of the total downward transport.

We observe a singularity at the MLD in Figures 11c,d. This is due to the total downward fluxes (not shown), which have a local extremum at this depth. At present, this maximum is not fully understood. We therefore focus on the two depths 0.9 MLD and 1.1 MLD to obtain a more robust description. As mentioned above, in 1A we observe a shift in the sign of ΣwC , from positive (i.e. obduction) to negative (i.e. subduction). Overall, the net fluxes near the MLD are close to 0, indicating that 1A does not contribute significantly to subduction, the absolute contribution being 1-5%. Conversely, the fluxes associated with 1C at the MLD are important and represent a significant contribution in terms of subduction, particularly during the winter and spring months, with a contribution of 30-40% of the total flux. There is a slight decrease in the contribution with depth, which again could be due to the limitation of the methodology. We find the evidence of a clear relationship between the tracer fluxes, the subduction contribution around the MLD, and the front density (Figures 11e-h). In particular, the subduction contribution in 1C shows a direct correlation with the front density ($r^2 = 0.90-0.92$). The linear relationship is also observed for the anticyclonic front, but not as effective ($r^2 = 0.66-0.74$). This results suggests that, in this region, the frontal contribution and associated flux can be estimated from the surface strain-vorticity front signature.

5 Discussion

5.1 Bias and futur improvements

Few studies have used surface strain-vorticity statistical tools to characterise submesoscale dynamics in both observations and models (Shcherbina et al., 2013; Rocha et

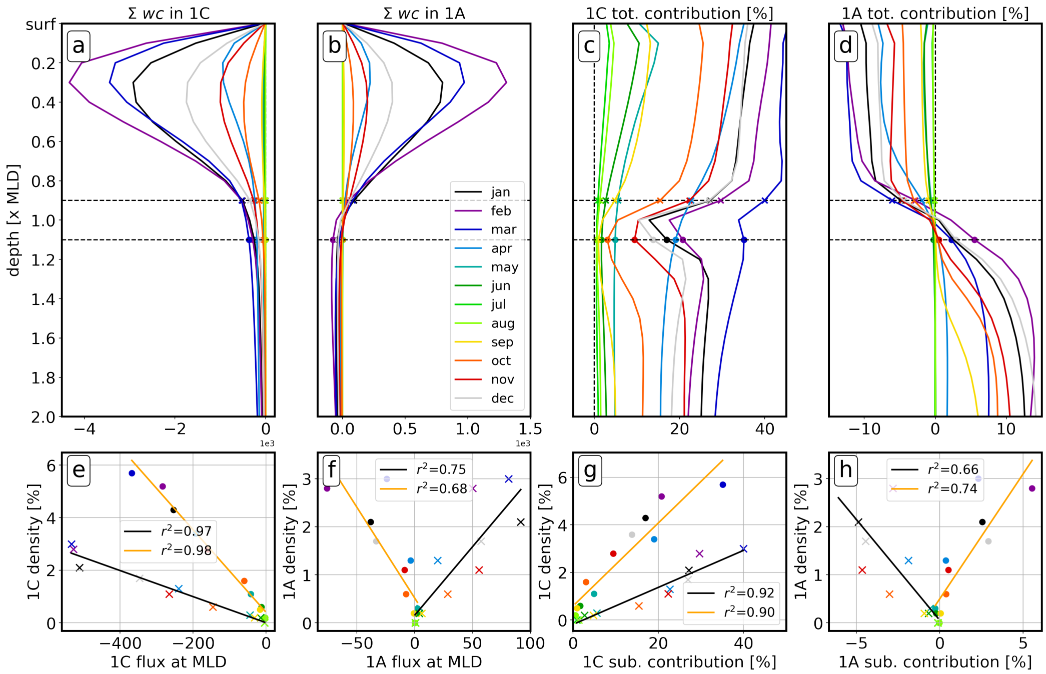

Figure 11. Net fluxes in 1C (a) and 1A (b) between surface and 2 * MDL. Total negative flux contribution for 1C (c) and 1A (d). Corresponding linear regressions between frontal area and fluxes at MLD / total subduction contribution are given for 1C (e,g) and 1A (f,h).

al., 2016; Balwada et al., 2021; Vic et al., 2022; Wang et al., 2022). To our knowledge, Balwada et al. (2021) is the only study using JPDFs and tracer vertical transport conditioned on surface strain and vorticity to estimate the submesocale frontal contribution at depth. As mentionned in Balwada et al. (2021), it is important to note that results from numerical simulations can be highly sensitive to the grid resolution, but also the output frequency (Figure B1). Due to numerical storage constraints, we chose here to use 3-h averaged outputs, but it is worth noting that these outputs slightly smoothed the frontal impact compared to hourly snapshots, resulting in a 0.5% loss in density. Therefore, our results may underestimate the effecs of the front on tracer transport.

One important limitation of this method is the connection between the surface dynamics and the dynamics at depth, as mentioned in section 3.2. In particular, the vertical velocities induced by a front are limited in depth and do not always follow a 1D vertical direction. Furthermore, the vertical structure of the fronts can be more complex and is not always surface intensified, as discussed in Wang et al. (2022). These limitations result in a bias that may be depth dependent and needs to be properly quantified in order to better understand the limited zone where such a method can be applied. This implies that the frontal isopycnal paths need to be accurately determined, which is a challenging task that remains to be addressed.

Finally, the definitions of the submesoscale frontal regions 1A and 1C used here are based on simplified assumptions. While these definitions provide reasonable approximations for estimating the initial impact of submesoscale fronts, they require further refinement. In reality, the definition of a submesoscale frontal region is more complex and may depend on the dynamics itself. Buckingham et al. (2016) demonstrated that ζ values in submesoscale regions are influenced by the Coriolis frequency and by the ratio of lateral to vertical buoyancy gradients. The Ro criteria used in our study may not be fully ap-

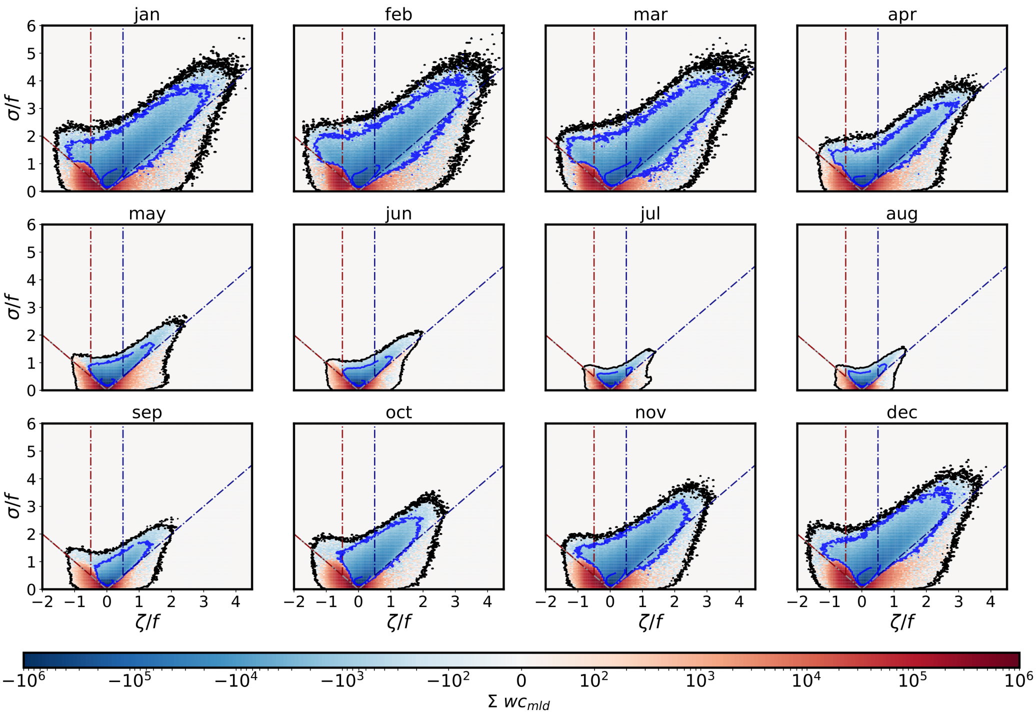

Figure 12. The sum of vertical advection $\Sigma w_{mld} \cdot C_{mld}$ conditioned by surface vorticity and strain. Integrated blue contours indicate 99% and 50% of the total negative flux. The black contour contains 99.99% of the points (points outside have been hidden).

propriate in certain regions, such as the Gulf Stream, where *Ro* is about 0.7–1.0 at the submesoscale, exceeding the values in our region. Therefore, we highlight the need for further theoretical development to precisely define a submesoscale zone within the surface strain-vorticity space. This will be crucial in the future for accurate estimation of tracer export influenced by submesoscale dynamics.

However, compared to previous studies, we observe similar associations between surface properties and transport at the MLD, and we also find similar orders of magnitude in terms of submesoscale contributions, reinforcing our confidence in the results.

5.2 Towards a better parameterization of the effect of fronts on tracer subduction

The main objective of this study was to gain a better understanding of the contribution of fronts to water subduction in a seasonal perspective. Proper quantification of subduction is crucial for understanding complex ocean mechanisms such as the carbon pump and heat transfer. Our seasonal study has allowed us to clearly identify front signatures and evaluate their impact on the transport of upper layer water to depth. Significant variations in front density allow us to infer a parameterization of the impact of fronts on tracer transport based solely on their surface characteristics. An important result is that the vertical advective subduction contribution can be estimated directly from the surface dynamics. So far, satellites have not been able to detect submesoscale features (Ballarotta et al., 2019). However, with the ongoing Surface Water and Ocean Topography (SWOT) mission (Fu & Ubelmann, 2014), it will soon be possible to improve the altimetry resolution to 10-30 km. This will allow better determination of front density and associated subduction rates, which is particularly relevant for biogeochemical studies focusing on the contribution of submesoscale features to the biological carbon pump, often referred to as the eddy-subduction pump (Boyd et al., 2019). Submesoscale processes capable of injecting particles to depth have not been clearly quantified yet, and this may partly explain why the carbon demand of the mesopelagic ecosystem exceeds the downward flux of presumably sinking POC by a factor of 2-3 (Burd et al., 2010). While this study used a simplified approach with homogenized tracer initialization within the ML, the same methodology could be adapted to study the front's contribution to carbon export and nutrient injection using coupled biochemical modeling. In addition, it is important to note that the seasonal results presented here are based on one year of data, and inter-annual variability can be significant (Berta et al., 2020). Further studies are needed to assess the sensitivity associated with different time periods, regions, and numerical models.

6 Conclusion

The present study investigates the seasonal fate of a passive tracer released monthly in the surface mixed layer using a realistic high-resolution simulation in the North Atlantic. Using surface strain and vorticity criteria, we identified and quantified the areas occupied by fronts and the density of frontsfor each month in 2008. Our observations revealed a deep sinking of the tracer in the presence of submesoscale activity and a consistent correlation between front density and tracer sinking emerged, independent of the mixed layer depth evolution. Remarkably, our investigation revealed that cyclonic submesoscale fronts, ranging from 0.5% in summer to about 6% in winter, contribute significantly to the total vertical advective subduction, ranging from 0.5% to 40%, respectively. These results not only confirm the efficacy of using surface vorticity-strain criteria for front analysis, but also emphasize the need to study fronts from a seasonal perspective.

Appendix A Front scheme

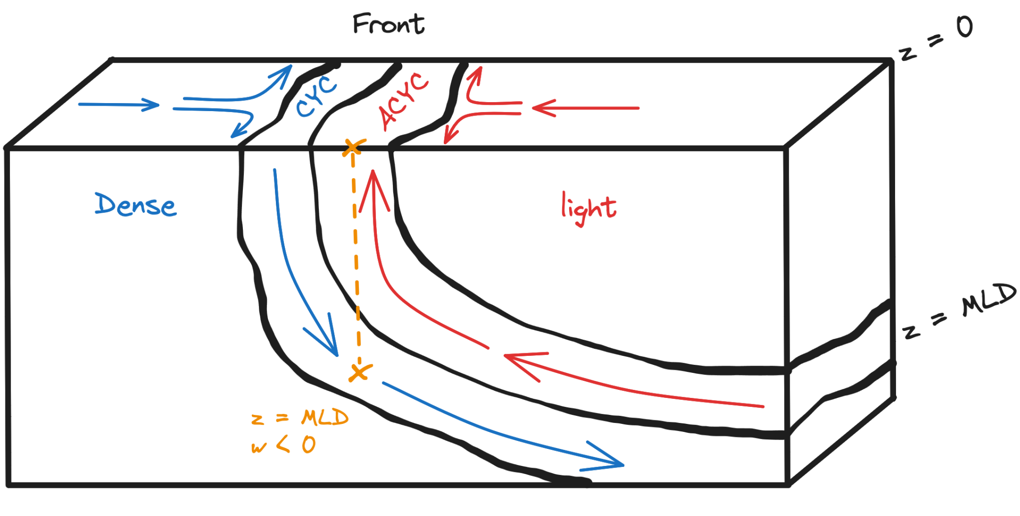

Figure A1. Scheme of a front cross-section. The orange cross represents the observation point. In this particular case, the vertical velocity below the surface anticyclonic front is not associated with an upwelling at z=MLD due to the slope of the front. This leads to a bias in our statistical results around and below the MLD.

Appendix B Time-averaged outputs sensibility

We have compared the JPDF and the 1C density during the first 5 days of March with different output frequencies. The figure B1 shows a significant difference between daily-averaged (1.6% of cyclonic front density) and hourly averaged or snapshot outputs ($>$ 5% of cyclonic front density).

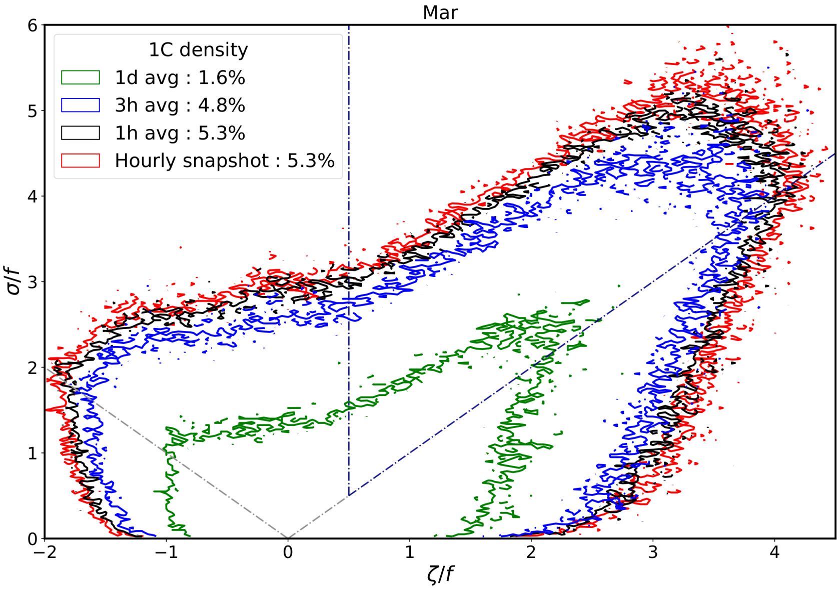

Figure B1. Surface strain-vorticity JPDF for 4 different output types which are daily averaged (green), 3-hour averaged (blue), 1-hour averaged (black) and hourly snapshot (red). The black contour is the integrated domain containing 99.99% of the points. The fraction of points within 1C is computed for each JPDF.

Acknowledgments

T.P. received a Ph.D. grant from École Normale Superieure Paris-Saclay. This work was also supported by the ISblue project, an Interdisciplinary graduate school for the blue planet (ANR-17-EURE-0015), and co-funded by a grant from the French government under the program "Investissements d'Avenir". J.G. would like to acknowledge support from the French National Agency for Research (ANR) through the project DEEPER (ANR-19-CE01-0002-01). Simulations were performed using HPC resources from GENCI-TGCC (Grants 2022-A0090112051), and from HPC facilities DATARMOR of "Pôle de Calcul Intensif pour la Mer" at Ifremer Brest France.

References

Ballarotta, M., Ubelmann, C., Pujol, M. I., Taburet, G., Fournier, F., Legeais, J. F., … Picot, N. (2019, aug). On the resolutions of ocean altimetry maps. *Ocean Science*, *15*(4), 1091–1109. doi: 10.5194/os-15-1091-2019

Balwada, D., Smith, K. S., & Abernathey, R. (2018, sep). Submesoscale Vertical Velocities Enhance Tracer Subduction in an Idealized Antarctic Circumpolar Current. *Geophysical Research Letters*, *45*(18), 9790–9802. Retrieved from `https://agupubs.onlinelibrary.wiley.com/doi/10.1029/2018GL079244` doi: 10.1029/2018GL079244

Balwada, D., Xiao, Q., Smith, S., Abernathey, R., & Gray, A. R. (2021, jun). Vertical fluxes conditioned on vorticity and strain reveal submesoscale ventilation. *Journal of Physical Oceanography*. doi: 10.1175/jpo-d-21-0016.1

Barkan, R., Molemaker, M. J., Srinivasan, K., McWilliams, J. C., & D'asaro, E. A. (2019, jun). The role of horizontal divergence in submesoscale frontogenesis. *Journal of Physical Oceanography*, *49*(6), 1593–1618. doi: 10.1175/JPO-D-18-0162.1

Berta, M., Griffa, A., Haza, A. C., Horstmann, J., Huntley, H. S., Ibrahim, R., ... Poje, A. C. (2020, oct). Submesoscale Kinematic Properties in Summer and Winter Surface Flows in the Northern Gulf of Mexico. *Journal of Geophysical Research: Oceans*, *125*(10), e2020JC016085. Retrieved from `https://agupubs.onlinelibrary.wiley.com/doi/10.1029/2020JC016085` doi: 10.1029/2020JC016085

Bol, R., Henson, S. A., Rumyantseva, A., & Briggs, N. (2018, dec). High-Frequency Variability of Small-Particle Carbon Export Flux in the Northeast Atlantic. *Global Biogeochemical Cycles*, *32*(12), 1803–1814. doi: 10.1029/2018GB005963

Bopp, L., Resplandy, L., Orr, J. C., Doney, S. C., Dunne, J. P., Gehlen, M., ... Vichi, M. (2013). Multiple stressors of ocean ecosystems in the 21st century: Projections with CMIP5 models. *Biogeosciences*, *10*(10), 6225–6245. doi: 10.5194/bg-10-6225-2013

Boyd, P. W., Claustre, H., Levy, M., Siegel, D. A., & Weber, T. (2019). Multi-faceted particle pumps drive carbon sequestration in the ocean. *Nature*, *568*(7752), 327–335. doi: 10.1038/s41586-019-1098-2

Buckingham, C. E., Naveira Garabato, A. C., Thompson, A. F., Brannigan, L., Lazar, A., Marshall, D. P., ... Belcher, S. E. (2016). Seasonality of submesoscale flows in the ocean surface boundary layer. *Geophysical Research Letters*, *43*(5), 2118–2126. doi: 10.1002/2016GL068009

Burd, A. B., Hansell, D. A., Steinberg, D. K., Anderson, T. R., Arístegui, J., Baltar, F., ... Tanaka, T. (2010, aug). Assessing the apparent imbalance between geochemical and biochemical indicators of meso- and bathypelagic biological activity: What the @$! is wrong with present calculations of carbon budgets? *Deep-Sea Research Part II: Topical Studies in Oceanography*, *57*(16), 1557–1571. doi: 10.1016/j.dsr2.2010.02.022

Callies, J., Ferrari, R., Klymak, J. M., & Gula, J. (2015). Seasonality in submesoscale turbulence. *Nature Communications*, *6*(1), 6862. Retrieved from `https://doi.org/10.1038/ncomms7862` doi: 10.1038/ncomms7862

Cao, H., & Jing, Z. (2022, feb). Submesoscale ageostrophic motions within and below the mixed layer of the northwestern Pacific Ocean. *Journal of Geophysical Research: Oceans*. Retrieved from `https://onlinelibrary.wiley.com/doi/10.1029/2021JC017812` doi: 10.1029/2021JC017812

Capet, X., Campos, E. J., & Paiva, A. M. (2008, aug). Submesoscale activity over the Argentinian shelf. *Geophysical Research Letters*, *35*(15), L15605. Retrieved from `http://doi.wiley.com/10.1029/2008GL034736` doi: 10.1029/2008GL034736

Chelton, D. B., Schlax, M. G., & Samelson, R. M. (2011, oct). Global observations of nonlinear mesoscale eddies. *Progress in Oceanography*, *91*(2), 167–216. doi: 10.1016/j.pocean.2011.01.002

de Boyer Montégut, C., Madec, G., Fischer, A. S., Lazar, A., & Iudicone, D. (2004, dec). Mixed layer depth over the global ocean: An examination of profile data and a profile-based climatology. *Journal of Geophysical Research*, *109*(C12), C12003. Retrieved from `http://doi.wiley.com/10.1029/2004JC002378` doi: 10.1029/2004JC002378

Fox-Kemper, B., Adcroft, A., Böning, C. W., Chassignet, E. P., Curchitser, E., Danabasoglu, G., ... Yeager, S. G. (2019, feb). *Challenges and prospects* *in ocean circulation models* (Vol. 6) (No. FEB). Frontiers Media S.A. doi: 10.3389/fmars.2019.00065

Freilich, M., & Mahadevan, A. (2021, may). Coherent Pathways for Subduction From the Surface Mixed Layer at Ocean Fronts. *Journal of Geophysical Research: Oceans*, *126*(5), e2020JC017042. Retrieved from `https://onlinelibrary.wiley.com/doi/10.1029/2020JC017042` doi: 10.1029/2020JC017042

Fu, L. L., & Ubelmann, C. (2014, feb). On the transition from profile altimeter to swath altimeter for observing global ocean surface topography. *Journal of Atmospheric and Oceanic Technology*, *31*(2), 560–568. doi: 10.1175/JTECH-D-13-00109.1

Gula, J., Molemaker, J. J., & Mcwilliams, J. C. (2014). Submesoscale cold filaments in the Gulf Stream. *Journal of Physical Oceanography*, *44*(10), 2617–2643. doi: 10.1175/JPO-D-14-0029.1

Gula, J., Taylor, J., Shcherbina, A., & Mahadevan, A. (2021, jan). Submesoscale processes and mixing. In *Ocean mixing: Drivers, mechanisms and impacts* (pp. 181–214). Elsevier. doi: 10.1016/B978-0-12-821512-8.00015-3

Gula, J., Theetten, S., Cambon, G., & Roullet, G. (2021, June). *Description of the gigatl simulations.* Zenodo. Retrieved from `https://doi.org/10.5281/zenodo.4948523` doi: 10.5281/zenodo.4948523

J. J. Becker D. T. Sandwell, W. H. F. S. J. B. B. B. J. D. D. F. J. F. S. I. S.-H. K. R. L. K. M. S. N. A. P. R. T. J. V. R. G. W., & Weatherall, P. (2009). Global Bathymetry and Elevation Data at 30 Arc Seconds Resolution: SRTM30_PLUS. *Marine Geodesy*, *32*(4), 355–371. Retrieved from `https://doi.org/10.1080/01490410903297766` doi: 10.1080/01490410903297766

Klein, P., & Lapeyre, G. (2009). *The oceanic vertical pump induced by mesoscale and submesoscale turbulence* (Vol. 1). doi: 10.1146/annurev.marine.010908.163704

Lacour, L., Briggs, N., Claustre, H., Ardyna, M., & Dall'Olmo, G. (2019, mar). The Intraseasonal Dynamics of the Mixed Layer Pump in the Subpolar North Atlantic Ocean: A Biogeochemical-Argo Float Approach. *Global Biogeochemical Cycles*, *33*(3), 266–281. doi: 10.1029/2018GB005997

Lapeyre Guillaume, K. P. (2006). *Impact of the small-scale elongated filaments on the oceanic vertical pump* (Vol. 64) (Article No. 6). FRANCE. Retrieved from `https://archimer.ifremer.fr/doc/00000/2459/` doi: https://doi.org/10.1357/002224006779698369

Large, W. G., McWilliams, J. C., & Doney, S. C. (1994, nov). Oceanic vertical mixing: A review and a model with a nonlocal boundary layer parameterization. *Reviews of Geophysics*, *32*(4), 363. Retrieved from `http://doi.wiley.com/10.1029/94RG01872` doi: 10.1029/94RG01872

Le Corre, M., Gula, J., & Tréguier, A. M. (2020, apr). Barotropic vorticity balance of the North Atlantic subpolar gyre in an eddy-resolving model. *Ocean Science*, *16*(2), 451–468. doi: 10.5194/os-16-451-2020

Lévy, M., Couespel, D., Haëck, C., Keerthi, M., Mangolte, I., & Prend, C. J. (2024). The Impact of Fine-Scale Currents on Biogeochemical Cycles in a Changing Ocean. *Annual Review of Marine Science*, *16*(1), 1–25. doi: 10.1146/annurev-marine-020723-020531

Lévy, M., Franks, P. J., & Smith, K. S. (2018, dec). *The role of submesoscale currents in structuring marine ecosystems* (Vol. 9) (No. 1). Nature Publishing Group. doi: 10.1038/s41467-018-07059-3

Llort, J., Langlais, C., Matear, R., Moreau, S., Lenton, A., & Strutton, P. G. (2018). Evaluating Southern Ocean Carbon Eddy-Pump From Biogeochemical-Argo Floats. *Journal of Geophysical Research: Oceans*, *123*(2), 971–984. doi: 10.1002/2017JC012861

Mahadevan, A. (2016, jan). The Impact of Submesoscale Physics on Primary

Productivity of Plankton. *Annual Review of Marine Science*, *8*(1), 161–184. Retrieved from `https://www.annualreviews.org/doi/10.1146/annurev-marine-010814-015912` doi: 10.1146/annurev-marine-010814-015912

Mahadevan, A., Pascual, A., Rudnick, D. L., Ruiz, S., Tintoré, J., & D'Asaro, E. (2020, jan). Coherent pathways for vertical transport from the surface ocean to interior. *Bulletin of the American Meteorological Society*, *101*(11), E1996–E2004. doi: 10.1175/BAMS-D-19-0305.1

Mahadevan, A., & Tandon, A. (2006). An analysis of mechanisms for submesoscale vertical motion at ocean fronts. *Ocean Modelling*, *14*(3-4), 241–256. doi: 10.1016/j.ocemod.2006.05.006

McWilliams, J. C. (2016, may). *Submesoscale currents in the ocean* (Vol. 472) (No. 2189). Royal Society of London. doi: 10.1098/rspa.2016.0117

McWilliams, J. C. (2021, jan). Oceanic Frontogenesis. *Annual Review of Marine Science*, *13*(1), 227–253. Retrieved from `https://www.annualreviews.org/doi/10.1146/annurev-marine-032320-120725` doi: 10.1146/annurev-marine-032320-120725

Omand, M. M., D'Asaro, E. A., Lee, C. M., Perry, M. J., Briggs, N., Cetinić, I., & Mahadevan, A. (2015). Eddy-driven subduction exports particulate organic carbon from the spring bloom. *Science*, *348*(6231), 222–225. doi: 10.1126/science.1260062

Pietri, A., Capet, X., D'ovidio, F., Levy, M., Sommer, J. L., Molines, J. M., & Giordani, H. (2021, mar). Skills and limitations of the adiabatic omega equation: How effective is it to retrieve oceanic vertical circulation at mesoscale and submesoscale? *Journal of Physical Oceanography*, *51*(3), 931–954. doi: 10.1175/JPO-D-20-0052.1

Ratner, B. (2009, jun). The correlation coefficient: Its values range between 1/1, or do they. *Journal of Targeting, Measurement and Analysis for Marketing*, *17*(2), 139–142. doi: 10.1057/jt.2009.5

Rocha, C. B., Gille, S. T., Chereskin, T. K., & Menemenlis, D. (2016, nov). Seasonality of submesoscale dynamics in the Kuroshio Extension. *Geophysical Research Letters*, *43*(21), 11,304–11,311. doi: 10.1002/2016GL071349

Saha, S., Moorthi, S., Pan, H.-L., Wu, X., Wang, J., Nadiga, S., ... Goldberg, M. (2010). The NCEP Climate Forecast System Reanalysis. *Bulletin of the American Meteorological Society*, *91*(8), 1015–1058. Retrieved from `https://journals.ametsoc.org/view/journals/bams/91/8/2010bams3001_1.xml` doi: https://doi.org/10.1175/2010BAMS3001.1

Sanders, R., Henson, S. A., Koski, M., De La Rocha, C. L., Painter, S. C., Poulton, A. J., ... Martin, A. P. (2014, dec). The Biological Carbon Pump in the North Atlantic. *Progress in Oceanography*, *129*(PB), 200–218. doi: 10.1016/j.pocean.2014.05.005

Shchepetkin, A. F., & McWilliams, J. C. (2005). The regional oceanic modeling system (ROMS): A split-explicit, free-surface, topography-following-coordinate oceanic model. *Ocean Modelling*, *9*(4). doi: 10.1016/j.ocemod.2004.08.002

Shcherbina, A. Y., D'Asaro, E. A., Lee, C. M., Klymak, J. M., Molemaker, M. J., & McWilliams, J. C. (2013, sep). Statistics of vertical vorticity, divergence, and strain in a developed submesoscale turbulence field. *Geophysical Research Letters*, *40*(17), 4706–4711. Retrieved from `http://doi.wiley.com/10.1002/grl.50919` doi: 10.1002/grl.50919

Siegelman, L., Klein, P., Rivière, P., Thompson, A. F., Torres, H. S., Flexas, M., & Menemenlis, D. (2020, jan). Enhanced upward heat transport at deep submesoscale ocean fronts. *Nature Geoscience*, *13*(1), 50–55. doi: 10.1038/s41561-019-0489-1

Siegelman, L. I. (2020, mar). Energetic submesoscale dynamics in the ocean interior. *Journal of Physical Oceanography*, *50*(3), 727–749. doi: 10.1175/JPO-D-19-0253.1

Stukel, M. R., Aluwihare, L. I., Barbeau, K. A., Chekalyuk, A. M., Goericke, R., Miller, A. J., ... Landry, M. R. (2017, feb). Mesoscale ocean fronts enhance carbon export due to gravitational sinking and subduction. *Proceedings of the National Academy of Sciences of the United States of America*, *114*(6), 1252–1257. Retrieved from `https://pnas.org/doi/full/10.1073/pnas.1609435114` doi: 10.1073/pnas.1609435114

Takahashi, T., Sutherland, S. C., Sweeney, C., Poisson, A., Metzl, N., Tilbrook, B., ... Nojiri, Y. (2002, jan). Global sea-air CO2 flux based on climatological surface ocean pCO2, and seasonal biological and temperature effects. *Deep-Sea Research Part II: Topical Studies in Oceanography*, *49*(9-10), 1601–1622. doi: 10.1016/S0967-0645(02)00003-6

Taylor, R. (1990, jan). Interpretation of the Correlation Coefficient: A Basic Review. *Journal of Diagnostic Medical Sonography*, *6*(1), 35–39. doi: 10.1177/875647939000600106

Treguier, A. M., Theetten, S., Chassignet, E. P., Penduff, T., Smith, R., Talley, L., ... Böning, C. (2005, may). The North Atlantic subpolar gyre in four high-resolution models. *Journal of Physical Oceanography*, *35*(5), 757–774. doi: 10.1175/JPO2720.1

Uchida, T., Balwada, D., Abernathey, R., McKinley, G., Smith, S., & Lévy, M. (2019, dec). The Contribution of Submesoscale over Mesoscale Eddy Iron Transport in the Open Southern Ocean. *Journal of Advances in Modeling Earth Systems*, *11*(12), 3934–3958. Retrieved from `https://agupubs.onlinelibrary.wiley.com/doi/10.1029/2019MS001805` doi: 10.1029/2019MS001805

Vic, C., Hascoët, S., Gula, J., Huck, T., & Maes, C. (2022). Oceanic Mesoscale Cyclones Cluster Surface Lagrangian Material. *Geophysical Research Letters*, *49*(4), e2021GL097488. Retrieved from `https://agupubs.onlinelibrary.wiley.com/doi/abs/10.1029/2021GL097488` doi: https://doi.org/10.1029/2021GL097488

Wang, L., Gula, J., Collin, J., & Mémery, L. (2022, jul). Effects of Mesoscale Dynamics on the Path of Fast-Sinking Particles to the Deep Ocean: A Modeling Study. *Journal of Geophysical Research: Oceans*, *127*(7), e2022JC018799. Retrieved from `https://onlinelibrary.wiley.com/doi/10.1029/2022JC018799` doi: 10.1029/2022JC018799

Wenegrat, J. O., Thomas, L. N., Sundermeyer, M. A., Taylor, J. R., D'Asaro, E. A., Klymak, J. M., ... Lee, C. M. (2020, jul). Enhanced mixing across the gyre boundary at the Gulf Stream front. *Proceedings of the National Academy of Sciences of the United States of America*, *117*(30), 17607–17614. doi: 10.1073/pnas.2005558117